CZECH TECHNICAL UNIVERSITY IN PRAGUE

FACULTY OF NUCLEAR SCIENCES AND PHYSICAL ENGINEERING

Department of Physics

Strange Particle Production in Jets in pp Collisions in the ALICE Experiment

MASTER'S THESIS

Bc. Vojtěch Pacík

Supervisor: RNDr. Jana Bielčíková, Ph.D.

Consultant: Mgr. Vít Kučera

Prague, 2016

ČESKÉ VYSOKÉ UČENÍ TECHNICKÉ V PRAZE
FAKULTA JADERNÁ A FYZIKÁLNĚ INŽENÝRSKÁ

Katedra fyziky

Produkce podivných částic v jetech v pp srážkách v experimentu ALICE

DIPLOMOVÁ PRÁCE

Bc. Vojtěch Pacík

Vedoucí práce: RNDr. Jana Bielčíková, Ph.D.

Konzultant: Mgr. Vít Kučera

Praha, 2016

Prohlášení

Prohlašuji, že jsem tuto práci vypracoval samostatně a použil jsem pouze podklady uvedené v přiloženém seznamu.

Nemám závažný důvod proti užití tohoto školního díla ve smyslu § 60 Zákona č. 121/2000 Sb., o právu autorském, o právech souvisejících s právem autorským a o změně některých zákonů (autorský zákon).

V Praze dne ....

Title: **Strange particle production in jets in pp collisions in the ALICE experiment**

Author: Bc. Vojtěch Pacík

Field: Experimental Nuclear and Particle Physics (Nuclear Engineering)

Document: Master Thesis

Supervisor: RNDr. Jana Bielčíková, Ph.D.
Nuclear Physics Institute, Czech Academy of Sciences.

Consultant: Mgr. Vít Kučera
Nuclear Physics Institute, Czech Academy of Sciences.

Abstract:

Enhancement of the baryon-meson ratio of the inclusive strange particles relative to proton-proton collisions was observed in the central heavy-ion collisions at RHIC and the LHC. Study of identified particles in jets can provide a unique way to investigate this phenomenon and disentangle the effects of the hot and dense medium created in ultra-relativistic collisions on various hadronisation processes and particle production mechanisms. In this thesis, the analysis of the K^0_S, Λ and $\overline{\Lambda}$ production in proton-proton collisions at the centre-of-mass energy $\sqrt{s} = 7$ TeV measured by the ALICE experiment at the LHC is presented. In particular, transverse momentum spectra and the baryon-meson ratios of strange particles associated with the charged jets as well as inclusively produced are reported. The comparison with the latest results of currently ongoing analyses in Pb-Pb and p-Pb collisions in the ALICE experiment is also presented.

Keywords: neutral strange particle, baryon anomaly, jets, ALICE, LHC

Název práce: **Produkce podivných částic v jetech v pp srážkách v experimentu ALICE**
Autor: Bc. Vojtěch Pacík

Obor: Jaderné inženýrství
Druh práce: Diplomová práce

Vedoucí práce: RNDr. Jana Bielčíková, Ph.D.
Ústav jaderné fyziky, Akademie věd České republiky, v.v.i.

Konzultant: Mgr. Vít Kučera
Ústav jaderné fyziky, Akademie věd České republiky, v.v.i.

Abstrakt:

Při centrálních srážkách těžkých iontů na urychlovačích RHIC a LHC bylo pozorováno navýšení poměru baryonů a mezonů vzhledem k proton-protonovým srážkám. Studium identifikovaných částic v jetech může poskytnout jedinečný způsob pro zkoumání tohoto jevu a odlišení vlivu horkého a hustého média vznikajícího při těchto ultra-relativistických srážkách vůči různým procesům hadronizace a mechanismům produkce částic. V této diplomové práci je popsána analýza produkce K^0_S, Λ a $\overline{\Lambda}$ částic v proton-protonových srážkách o těžišťové energii $\sqrt{s} = 7$ TeV změřené experimentem ALICE na urychlovači LHC. Zvláště pak spektra příčných hybností a baryon-mesonový poměr částic asociovaných s nabitými jety a inkluzivně produkovanými částicemi. Také je provedeno srovnání s aktuálními výsledky probíhajících analýz v Pb-Pb and p-Pb srážkách v experimentu ALICE.

Klíčová slova: neutrální podivné částice, baryonová anomálie, jety, ALICE, LHC

Acknowledgement

First and foremost, I would like to express my deepest gratitude to the person whose office door has been always open for me whenever an advice was needed or question arose for her expert guidance and all the fruitful discussions we have had during the last two years and also for providing me an opportunity to contribute to the ALICE Collaboration and the Heavy-Ion Group at Nuclear Physics Institute, my supervisor Jana Bielčíková. Without her, this thesis would not have even existed in the first place.

My sincere thanks to my consultant and brother-in-arms Vít Kučera for his unshakable patience while facing never ending line of questions related to the analysis and the topic of this thesis, his willingness and active cooperation whenever it was needed, many comments and suggestions how to improve my code, plots and presentations.

I would like also thank my friends and colleagues from the Nuclear Physics Institute of Czech Academy of Sciences and the FNSPE of Czech Technical University in Prague Jaroslav Adam, Pavol Federic, Jan Rusnak and Miroslav Šimko who assisted me many times during my struggle with coding and other technical related aspects of this work, for their critical feedback and constructive comments as well as interesting discussions and funny moments spend in the office or the cafeteria during the lunch. Additionally to that, my special thanks go to Filip Krizek for the final proofreading of this thesis with.

Last but not least, my thanks belong to the closest friends and my family for their undying support and continuous encouragement throughout my entire studies, for their kind, friendly and forgiving attitude, especially in the times when I was acting not so friendly. I will never be able to fully express how much I appreciate your presence in my life.

Thank you.

Contents

List of Figures

Preface

In heavy-ion (AA) collisions at the ultra-relativistic energies, such as those achieved at the Large Hadron Collider (LHC) at CERN or Relativistic Heavy Ion Collider (RHIC) at Brookhaven National Laboratory, a new state of strongly interacting nuclear matter consisting of deconfined quarks and gluons is expected to be formed. This state of matter called quark-gluon plasma (QGP) exists only for a very short time under the extreme conditions such as high temperature and/or density. As the conditions change due to the evolution of the bulk a phase transition occurs from these quasi-free partons to the observed final state hadrons where the partons are confined again.

The identification of hadrons and their transverse momentum (p_{T}) spectra and ratios provide a unique tool to study this new state of matter [1]. It was first observed at RHIC [2, 3], that the baryon-meson ratio is enhanced in central heavy-ion collisions in comparison with the peripheral or proton-proton (pp) collisions. This enhancement has been observed not only for light flavour hadrons containing u and d quarks, protons and pions, but also in the case of inclusive strange particles, Λ and $\mathrm{K}^0_{\mathrm{S}}$ generally known as the V^0 particles. Similar analysis of inclusive light flavour hadron production has been done later at the LHC at CERN, both in proton-proton and heavy-ion collisions [4].

This so-called "baryon anomaly" phenomenon is still not fully understood, although various theoretical models are currently under investigation, namely the parton fragmentation and the hadronisation modification [5], the parton recombination [6] and the radial flow [7].

The main motivation of this thesis is the study of neutral strange particle production in charged jets in pp collisions in order to provide a better understanding of the origin of the baryon anomaly. The results of pp analysis are therefore crucial to disentangle the effects of hot and dense strongly interacting medium created in heavy-ion collisions from mechanisms of particle production in cold nuclear matter. This can only be achieved by comparing identified hadrons associated with charged jets with those inclusively produced across all collision systems (pp, p-Pb and Pb-Pb).

This thesis is structured as follows. First, a brief introduction to the field of heavy-ion physics focusing on the quark-gluon plasma and its properties is given in Chapter 1. The basic physical concept of the jets and the methodology of various jet reconstruction algorithms is presented in Chapter 2. The baryon anomaly phenomenon is described in Chapter 3. In Chapter 4, the ALICE (A Large Ion Collider Experiment) detector, the only LHC experiment dedicated to the study of QGP properties, will be briefly described including the detection sub-systems involved in the conducted analysis. The topic of this thesis, the analysis of neutral strange $\mathrm{K}^0_{\mathrm{S}}$ and Λ particle production associated with charged jets as well as the inclusively produced in pp collisions at $\sqrt{s} = 7$ TeV, will be reported in detail in Chapter 5, followed by the results presented in Chapter 6.

Chapter 1

Quark-gluon plasma

The most of the matter in the visible Universe consists of the elementary particles called quarks. These fundamental building blocks are bound together inside the hadrons (composite particles such as for example protons or neutrons) via the intermediate gauge bosons, gluons. Behaviour of quarks and gluons, is governed by the strong nuclear interaction described by the theory of Quantum Chromodynamics (QCD).

The QCD is a non-Abelian gauge field theory based on the SU(3) symmetry group. It originated in the 1960's when Oscar W. Greenberg, Moo-Young Han and Yoichiro Nambu formulated the concept of the colour charge as an additional quantum degree of freedom [8] solving the issue with Δ^{++} baryon[1]. According to this theory, we distinguish three types of colour charge, which can be labelled, e.g. red, green and blue; and their conjugates: anti-red, anti-green, anti-blue. The strong interaction is mediated by the gluon exchange.

One of the basic concepts of the QCD is that contrary to the partons (general term for quarks and gluons) carrying colour charge, free particles have to be colourless or "white" in analogy with the visible light. Thus neither quarks nor gluons have been ever directly observed as single particles under the ordinary conditions. More precisely this is due to the potential of the strong interaction which increases with the increasing distance. Therefore when trying to separate two quarks from each other, the energy increases until the new pair of quark and anti-quark is created. This phenomenon is generally known as the confinement.

On the other hand, with the decreasing distance or increasing energy, the coupling constant of strong interaction logarithmically decreases and the bond between the quarks becomes asymptotically weaker. In this region, the parton can be treated as a quasi-free particle. It also allows to use the perturbation theory approach for theoretical calculations in the QCD (pQCD). Such property of the quantum field theory is referred to as the asymptotic freedom and the Nobel Prize in physics was awarded for its discovery to Frank Wilczek, David Gross and David Politzer in 2004 [9].

1.1 Ultra-relativistic heavy-ion collisions

As mentioned, the quarks and the gluons are normally bound within the hadrons. However, according to the discussed properties of the strong interaction, it is expected that under specific conditions a new state of the nuclear matter, where quarks and gluons are no longer confined, is formed. In order to achieve such conditions, extreme temperature and density is required. This very hot and dense medium, called the quark-gluon plasma (QGP), existed in the very early phases of the Universe, approximately 10^{-5} s after the Big Bang [10].

The alternative way how to create and subsequently study such unique environment have been made possible with the technological advancement in the field of the accelerators over the last few decades. Inside the enormous machines, such as the Large Hadron Collider

[1] This experimentally observed particle is composed of three *up* quarks with the parallel spin orientation. According to Pauli exclusion principle such quantum system cannot exists. And thus the need for additional degree of freedom has arisen.

(LHC) - the biggest synchrotron accelerator ever built - in the European Centre for Nuclear Physics (CERN) and Relativistic Heavy Ion Collider (RHIC) at Brookhaven National Laboratory (BNL), the beams of protons or nuclei are accelerated while circulating in the opposite direction. Then they are brought to the collisions inside the detectors located in several beam pipe intersections.

In case of heavy nuclei such as Pb or Au ions, maximal achievable collision energy in a nucleon pair centre of mass system $\sqrt{s}$ ranges from ~ 10 GeV up to ≈ 5 TeV per nucleon. At these energies, nuclei are moving at the velocity close to the speed of light in vacuum. Due to the effect of Lorentz contraction, they appear to be compressed along the direction of their movement. Therefore in the very moment of the collision, the participating nucleons from accelerated nuclei are almost immediately stopped and extremely high values of nucleon and energy densities are achieved and thus the QGP may be formed (in contrast to the proton-proton collisions, where the conditions are not sufficient). Such process is generally referred to as the ultra-relativistic heavy-ion collision.

1.2 Phase diagram of hadronic matter

The phase diagram of the hadronic matter, which scheme is depicted in Fig. 1.1, describes the phase transition between the ordinary matter and the QGP as a function of thermodynamic temperature T and baryochemical potential μ, which is related to the relative abundance of baryons and anti-baryons present in the system. The meaning of μ can be also explained as an amount of energy needed when an additional baryon is added into the system.

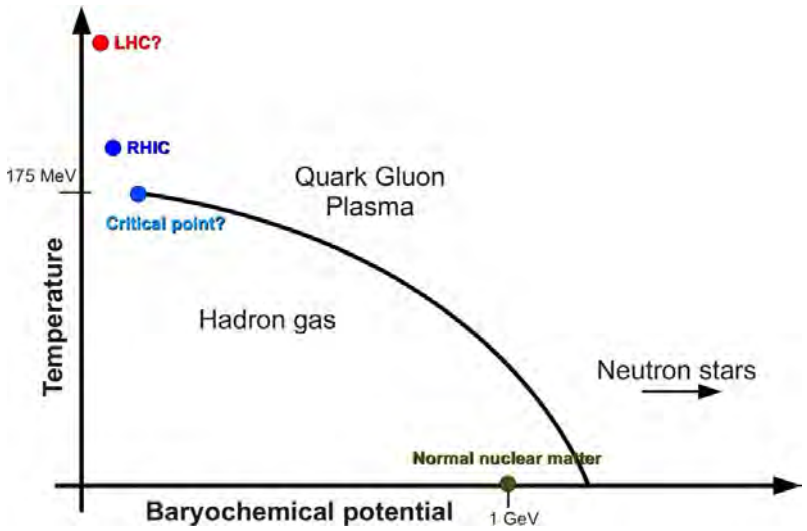

Figure 1.1: A scheme of a phase diagram of the hadronic matter as a function of system temperature T and baryochemical potential μ. The solid curve represents the first order phase transition between the QGP and the hardon gas ending with the critical point. Red and blue points indicate the approximate sensitivity region of the LHC and RHIC respectively. Taken from [11].

Under the normal conditions, the confined nuclear matter is in the thermodynamic region of low temperatures and relatively high baryochemical potential. As the temperature increases the binding energy is decreasing and the matter is in a state of hadron gas.

When the temperature and/or baryochemical potential is increasing even further, the phase transition between the hadron gas and the deconfined matter (QGP) occurs.

The current knowledge concerning the exact behaviour of such transition is still very limited and currently it is an object of intensive study. However in the region of non-zero baryochemical potential, the first order phase transition is expected which involves a latent heat. During the first order transition the system is in a mixed state and its temperature is constant until the transition is done (similarly to the ice melting or the boiling of water).

In the region of low baryochemical potential, after the critical point $[T_c; \mu_c]$ is reached, according to the results of lattice-QCD calculations, the rapid cross-over transition takes place [12]. The value of the critical temperature T_c was first estimated by Hagedorn's statistical model as $T_c \approx 170$ MeV [13] and later found to be in agreement with the lattice-QCD prediction. The recent experimental data from the ALICE experiment at the LHC obtained by fitting the measured yields of identified hadrons indicates $T_c \approx 150$ MeV [14]. The overview of the phase diagram obtained via the thermal fits from various experiments (and thus at various collision energies) is shown in Fig. 1.2.

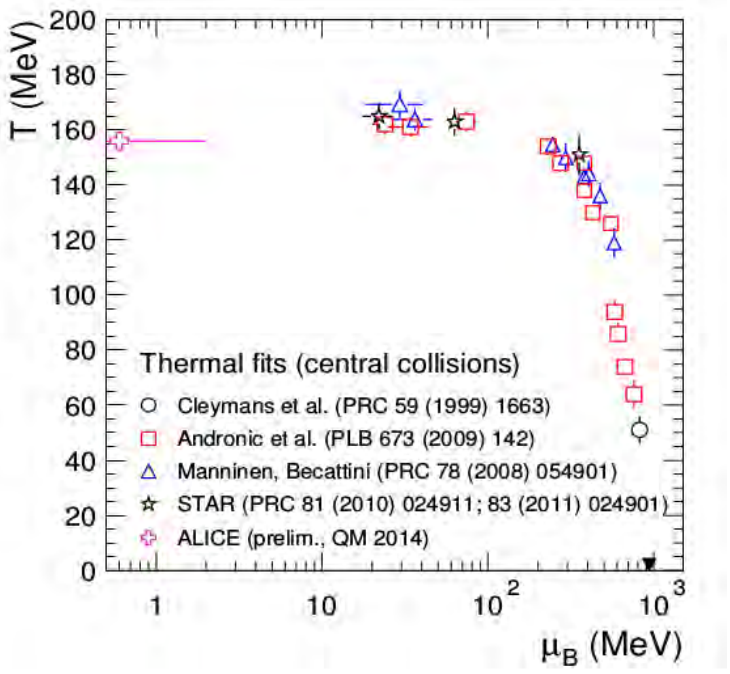

Figure 1.2: The phase diagram of the hadronic matter obtained from the thermal fits of the experimental data measured at various experiments covering wide range of the collisional energy. The black triangle represents the baryochemical potential of ordinary matter (nuclei) $\mu_0 = 931.4$ MeV. Taken from [14].

1.3 Space-time evolution of a heavy-ion collision

The space-time evolution [10] of the hot and dense medium, described in this section, can be divided into several subsequent steps as illustrated in Fig. 1.3. In the very moment of the collision the hardest processes, leading to creation of heavy flavour c, b quarks and high-p_{T} jets, take place. Then, as the two collided nuclei pass by, the extreme conditions described in previous section are established and thus the QGP could be formed. The

formation time τ_0, when the thermal equilibrium of the medium is expected, is less than 1 fm/c. In this stage the QGP can be sufficiently described by the hydrodynamics, since the behaviour of the plasma is similar to the ideal fluid [10].

As the QGP expands due to the presence of the pressure gradients, its temperature is decreasing until the discussed critical temperature T_c is achieved. In that moment, the medium undergoes a phase transition from the deconfined state to the hadron gas. This process is generally referred to as the hadronisation, during which the quasi-free quarks cluster into the observable baryons and mesons. As the temperature and density does not have to decrease homogeneously across the whole volume, hadronisation is not instantaneous.

In this stage, the inelastic scattering of the hadrons dominates until the mean distance between them gets large enough. After that point the chemical composition of the system is not changing much and the ratios of produced particles is fixed. This is called the chemical freeze-out T_{ch}. Following that, the elastic scattering of the particles takes over. Since the medium is still expanding, the density decreases and the mean free path is increasing until the hadron collisions cease completely and the kinetic properties are fixed, thus the kinetic freeze-out T_{fo} occurs. At this moment, the medium evolution ends and the resulting hadrons are present in the vacuum.

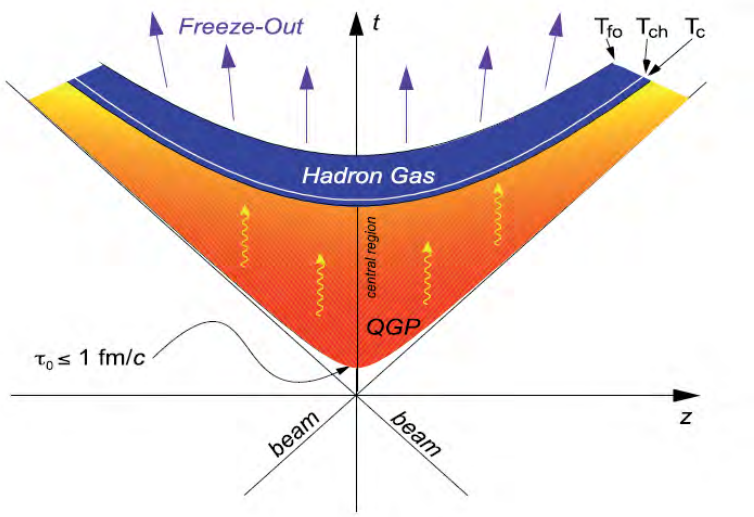

Figure 1.3: A light cone scheme of space-time evolution of the hot and dense medium formed during the ultra-relativistic collisions of heavy ions. The horizontal axis represents the longitudinal direction with respect to the beam axis, on vertical axis the time evolution is illustrated. More detailed description of the individual stages can be found within the text. Taken from [15].

1.4 Strangeness enhancement

As one of the first candidates for possible indication of the quark-gluon plasma formation, the enhancement of strangeness production with respect to the proton-proton collisions was proposed [16]. Nowadays, this phenomenon is rather generally interpreted as a consequence of the statistical hadronisation of thermalized medium [17].

Since in the initial state, prior to the collision, no valence strange content is present in the system (only protons or neutrons made of u and d quarks), all observed particles

containing strange quark have to be created as a direct consequence of the collision itself. Due to the conservation of strangeness in the strong interactions, s and $\bar{s}$ quarks are produced in the same number. When compared to the heavy-ion case, in small systems such as the proton-proton collision the strangeness production is more demanding. In this context, this phenomenon is generally referred to as canonical suppression of strangeness in small systems rather than enhancement in the heavy-ion collisions [18]. All together with the conservation of the baryon number, the anti-hyperons (baryons containing at least one (anti-)strange quark) are quite suitable probes of the QGP formation.

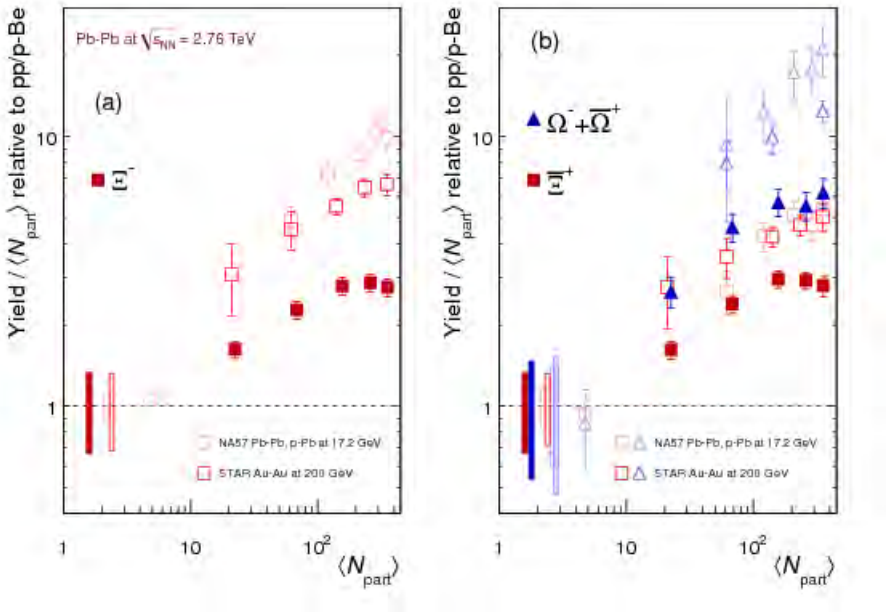

Figure 1.4: Yield of the multi-strange baryons produced in Pb-Pb collisions at $\sqrt{s_{\mathrm{NN}}} = 2.76$ TeV relative to the pp (or p-Be in case of SPS data) collisions as a function of the average number of the participants N_{part}. The LHC results are compared to the SPS and RHIC energies. Taken from [19].

The manifestation of such suppression is stronger as the overall strange content increases as shown in Fig. 1.4, where the recent results of multi-strange baryons Ξ and Ω (containing two and three strange (anti-)quarks respectively) yields produced in AA collision are presented. Since the number of participants can be related to the collision centrality, it also demonstrates that the enhancement is stronger in the more central collisions, where the larger volume of the hot and dense medium is expected to be created.

1.5 Jet quenching and nuclear modification factor

Another property of the medium created in heavy-ion collisions and the possible formation of the QGP is the so-called jet quenching phenomenon. As discussed in this section, the hardest processes, where the high-p_{T} partons (generally referred to as the hard probes) are created, occur in the initial stage of the collision. This happens even before the hot and dense medium is formed. Moments later, after the formation time, these high-p_{T} partons travel through the medium.

During this stage the probes interact with the medium and loss their energy via two major processes. The elastic collisions with the medium constituents dominate in the

region of low energies. As the probe energy increases, gluon radiation or *gluonstrahlung* becomes more and more significant. According to the dead-cone effect, the heavier quarks radiate less energy than the light quarks or gluons [20].

The amount of the energy loss depends not only on the properties of the parton but the medium as well [21], namely the parton path length traversed within the QGP. Therefore the measurements of high-p_{T} partons or heavy flavour quarks which were affected by the QGP play an important role when studying the properties of such unique environment.

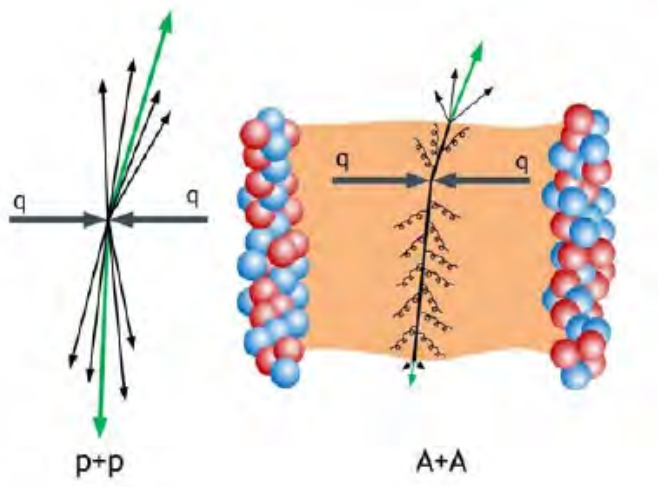

Figure 1.5: Illustration of jet quenching phenomenon. The comparison of the di-jet produced in the QCD vacuum (left) during the pp collision and the hot and dense medium (right) in a case of the heavy-ion collision. Taken from [15].

In order to describe the jet quenching, imagine that a $q\bar{q}$ pair of high-p_{T} quarks is created during the hard processes of proton-proton collision as illustrated in Fig. 1.5. Each of the two partons fragments into a shower of softer ones, which hadronise during the phase transition into the collimated showers of particles. From the experimental point-of-view this results in a pair of jets with similar energy, which are due to the momentum conservation oriented (almost) back-to-back (so-called di-jets).

Let us take a look on an analogous situation, but this time the original $q\bar{q}$ pair is created in the peripheral region of the nucleus-nucleus collision, where the QGP is formed, contrary to the pp case. Since one of the partons traverse longer distance through the medium, it ultimately loses more energy compared to the other parton. It may happen that this parton does not emerge from the QGP at all. This is the manifestation of the mentioned jet quenching.

For the proper quantification of such suppression of the high-p_{T} particles or jets, the nuclear modification factor R_{AA} is used. This rapidity (y) and momentum (p_{T}) dependent measure is generally defined as a ratio of the particle yields (or spectra) measured in the AA and the pp collisions scaled by the average number of binary nucleon-nucleon interactions experienced during heavy-ion collision parametrized by the nuclear overlap function T_{AA}:

$$R_{\mathrm{AA}}(b, y, p_T) = \frac{1}{\langle T_{\mathrm{AA}}(b) \rangle} \frac{\mathrm{d}^2 N_{\mathrm{AA}}/\mathrm{d}y\mathrm{d}p_T}{\mathrm{d}^2 N_{\mathrm{pp}}/\mathrm{d}y\mathrm{d}p_T}, \tag{1.1}$$

where the b is the impact parameter of the collision related to the event centrality. When the R_{AA} is close to the unity, the production in AA (pA) is similar to the pp collisions.

When it is lower, the production is considered suppressed with respect to the pp case or enhanced when the R_{AA} value is larger than 1.

In analogy to R_{AA}, the R_{CP} modification factor is defined as a ratio of yields (spectra) normalised by the number of binary collisions in central and peripheral heavy-ion collisions to quantify the effects of the medium:

$$R_{\mathrm{CP}}(y, p_T) = \frac{N_{\mathrm{bin}}^{\mathrm{peripheral}}}{N_{\mathrm{bin}}^{\mathrm{central}}} \frac{\mathrm{d}^2 N^{\mathrm{central}}/\mathrm{d}y\mathrm{d}p_T}{\mathrm{d}^2 N^{\mathrm{peripheral}}/\mathrm{d}y\mathrm{d}p_T}. \tag{1.2}$$

For the illustration of the nuclear modification the following figures are shown. First, the results of the open-charm (containing one $c/\bar{c}$ quark) D meson production measured by the ALICE experiment in Pb-Pb collision at $\sqrt{s_{\mathrm{NN}}} = 7$ TeV and p-Pb collisions at $\sqrt{s_{\mathrm{NN}}} = 5.02$ TeV is shown in Fig. 1.6, where . As can be seen, contrary to the production in the p-Pb system, which is similar to the pp, the Pb-Pb result exhibits relatively strong centrality dependent suppression.

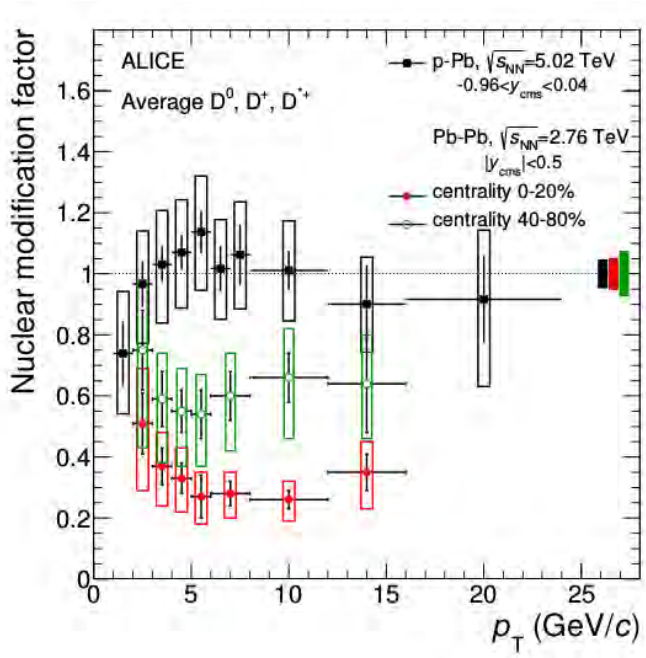

Figure 1.6: Nuclear modification factor of D meson production in p-Pb at $\sqrt{s_{\mathrm{NN}}} = 5.02$ TeV (black) and central (red) and periferal (green) Pb-Pb collisions at $\sqrt{s_{\mathrm{NN}}} = 7$ TeV as a function of p_{T}. Taken from [22].

Second, the nuclear modification factor R_{CP} of charged jets measured by the ATLAS and ALICE experiments illustrated in Fig. 1.7 exhibits a strong suppression by approximately factor of 2 in a wide region of $30 < p_{\mathrm{T}}^{\mathrm{jet,ch}} < 200$ GeV/c. The amount of charged jets suppression is similar to the charged hadrons results in p_{T} region $8 - 100$ GeV/c measured by ALICE and CMS [23].

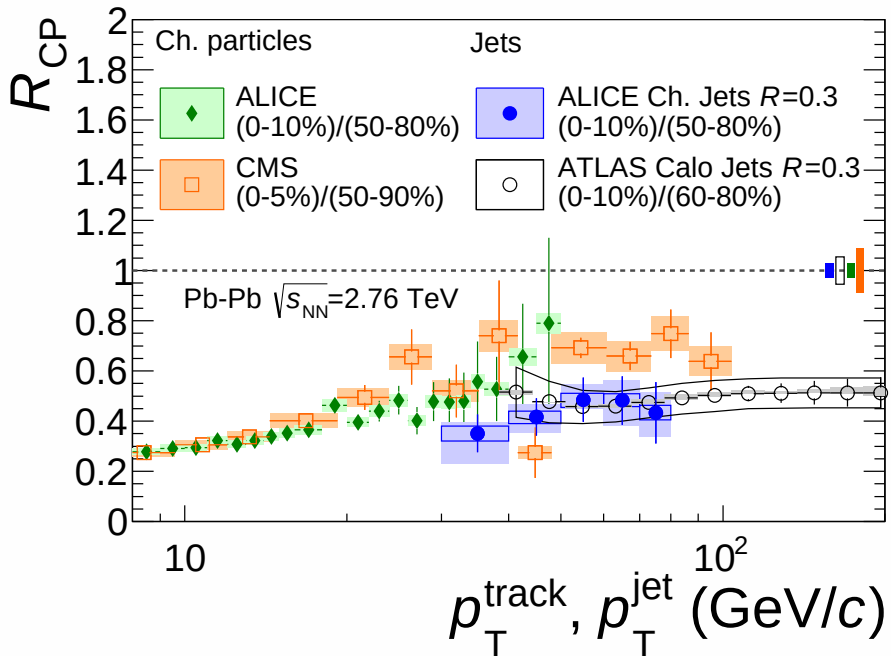

Figure 1.7: The comparison of R_{CP} of charged jets measured by the ATLAS and ALICE experiments and charged hadrons measured by ALICE and CMS produced in most central and peripheral Pb-Pb collisions at $\sqrt{s_{\mathrm{NN}}} = 2.76$ TeV. Taken from [23].

Chapter 2

Jets

According to the theory of the perturbative Quantum Chromodynamics (pQCD), a highly virtual parton can be created in a hard scattering occurring during the very first moments of the high-energy collision. These partons are not directly observable, instead one can observe jets, the collimated showers of particles resulting from the fragmentation and the hadronisation of the initially very energetic or hard[1] partons.

The proper reconstruction and the following physical interpretation of jets is therefore crucial for the correct understanding of the QCD aspects according to the current knowledge. From an experimental point of view searching for the sprays of collimated final state hadrons may seem like a rather trivial task, especially in case of the proton-proton collisions, where multiplicities are relatively low with respect to the collisions of heavy ions. But for the accurate comparison of the predictions at the parton level and experimentally observable particles, a well-defined jet-finding procedure is essential.

The jet-finding procedure begins with a list of "particles". These can be partons on the level of theoretical simulation or hadrons registered as a signal on the detector level (e.g. particle tracks or energy deposited in calorimeters). Particles that are close to each other in terms of the azimuthal and the polar angles are generally called clusters and are generally good candidates to originate form the same initial parton. The purpose of the jet finding algorithm (jet finder) is to select and associate particles and clusters into more complex objects - jets - according to the certain well-defined rules. This part of jet finder is called "jet algorithm". The kinematic properties of particles such as four-momentum have to be assigned to a jet as well. This is called a "recombination scheme". The difference between various jet finders is therefore given by using a specific jet algorithm and/or recombination scheme.

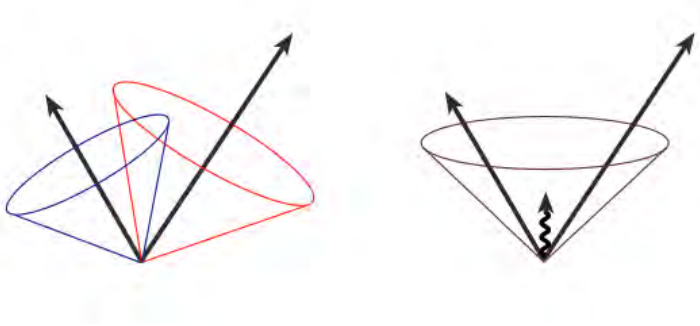

Figure 2.1: Illustration of infrared sensitivity. On the left hand side, two reconstructed jets can be seen. Adding soft radiation (in this example, low-p_{T} gluon) may change the outcome of the recombination procedure, as can be seen on the right hand side, where only one jet is reconstructed instead of the original two. Taken from [24].

For an ideal jet finder following features are necessary. The first one is infrared safety.

[1] Hard in a sense of high momentum transfer from which high-p_{T} particles are created. On the other hand, particles or partons with relatively low p_{T} is considered as soft.

Final jets resulting from the jet reconstruction procedure should be insensitive to any soft radiation, meaning that the addition or subtraction of a single hadron with low p_{T} should not change the properties of the reconstructed jet, such as shape or direction of its axis, as can be seen in Fig. 2.1.

The second one is collinear safety illustrated in Fig. 2.2. Imagine a single parton shower that is at the detector level registered as two independent signals separated by the almost zero distance, for instance in two neighbouring calorimeter cells. Such signals may in general change the resulting jet or not be identified as a jet at all (i.e. they not pass the energy threshold needed for distinguishing detector noise from the signal).

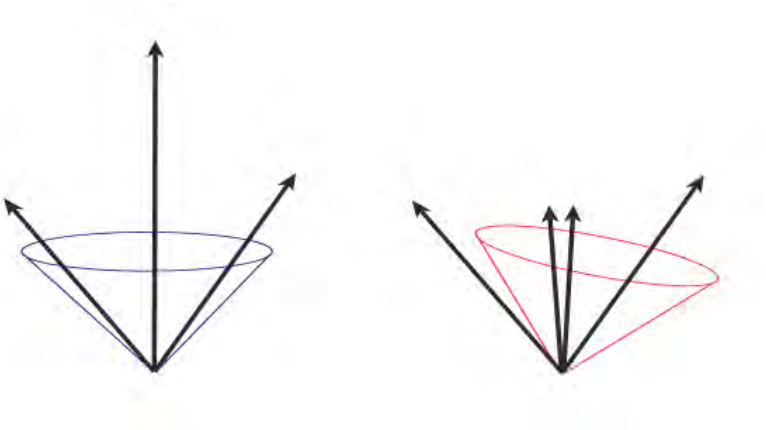

Figure 2.2: Illustration of collinear sensitivity. Registered signal (such as the middle one on the left hand side) may be registered as two independent signals due to the technical specifications of the detector, e.g. in two neighbouring calorimeter cells, as can be seen on the right hand side. This can therefore clearly affect the properties of the resulting jet. Taken from [24].

In addition, the ideal jet algorithm should be invariant under Lorentz boost in longitudinal direction, its reconstruction solution should be the same at parton, particle and detector level and also should be experiment and detector independent. Last but not least, considering the large amount of data expected to be processed, it should be as efficient as possible from the point of view of the computing time.

In general, one can distinguish two types of jet-finding algorithms, cone and sequential recombination algorithms [24] which are discussed in in more detail below.

2.1 Cone algorithms

The basic idea of the jet cone algorithm is to associate particles in a circular area with a specific radius R in $\phi \times \eta$ space, where ϕ is the azimuthal angle and η is the pseudorapidity given by $\eta = -\ln \tan \frac{\theta}{2}$, where θ is the polar angle.

For each circle, its energy weighted centroid is estimated (i.e. according to the energy distribution of the particles within the area), which becomes a new geometric centre of the circle. With respect to the particles in this new area, a new centroid is estimated. This process continues until a stable cone is found meaning that the geometric centre of the circular area is aligned with the centroid of energy deposition in the centre.

This rather simple jet finding algorithm could scan the whole detector and find all stable cones by simply using each space point as the initial centre. However, this may

turn out to be a quite time consuming process due to the large granularity of the current detectors and high number of particles. Therefore, the need for selecting more physically important starting points had arisen and the idea of so-called seeds was introduced [24] in order to reduce the required CPU time.

In case of cone algorithms with seeds, $\phi \times \eta$ space is scanned and all particles with energy larger than the specified threshold are tagged as seeds. These seeds are then used as the initial geometric centres, starting points of the jet algorithm. Although the seed algorithm is much faster than the seedless one, there is also a problem with such algorithm. The cone algorithm with seed is not collinear safe and is also quite sensitive to soft radiation. Situation may be improved by adding the so-called midpoints in between the seeds[2].

The remaining issue with the algorithms, both using seeds and seedless ones, that should be noted here is the fact, that the particles may be associated with more than one jet reconstructed with the cone algorithm. Overlapping cones need to be merged or split in order to solve this physical problem. Basic condition to decide whether the two overlapping cones should be merged or not is based on a shared energy fraction f relative to the one with less energy. If the less energetic cone shares more than f of its energy, two cones are merged, otherwise they are split according to the distance of shared particles.

One of the most commonly used cone algorithms is the SISCone. This seedless cone algorithm is not only infrared but also collinear safe in all orders of the perturbation theory [25]. SISCone searches for all possible stable cones, even though it is a relatively fast algorithm (with the complexity of $N^2 \log N$), for the large number of initial particles is still rather impractical.

2.2 Sequential recombination algorithms

The sequential recombination algorithms have been developed in contrast to the cone algorithms. These algorithms are successively merging pairs of particles in order related to their transverse momentum p_{T}.

First, the list of all particles (also known as pre-clusters) is created and four-momentum $(E_i, \overrightarrow{p_i})$ is assigned to each of them. For each pair of particles $(i, j), i \neq j$, parameter d_{ij} is defined in following way

$$d_{ij} = \min(p_{\mathrm{T},i}^{2p}, p_{\mathrm{T},j}^{2p}) \frac{\Delta R^2}{R^2}, \tag{2.1}$$

where ΔR (Eq. 2.2) is the distance between the particles in the $\eta \times \phi$ space. The R is a jet resolution parameter,

$$\Delta R = \sqrt{(\eta_i - \eta_j)^2 + (\phi_i - \phi_j)^2}, \tag{2.2}$$

which is similar to the cone radius and reflects the approximate area of the jet. Contrary to the rather circular cones, jets reconstructed via sequential recombination algorithms do not exhibit fixed conical shape (see Fig. 2.3). The power of p_{T} is $p = 1$ for k_{T} algorithm, $p = -1$ for anti-k_{T} algorithm and $p = 0$ for Cambridge-Aachen algorithm.

For each particle parameter d_i given by $d_i = p_{\mathrm{T},i}^2$ is estimated. Then the minimum d_{min} is found among d_{ij} and d_i of all particles.

[2] In practice, midpoints may be placed in the positions $p_i + p_j$ or $p_i + p_j + p_k$, where p_i, p_j, p_k are seeds four-momenta.

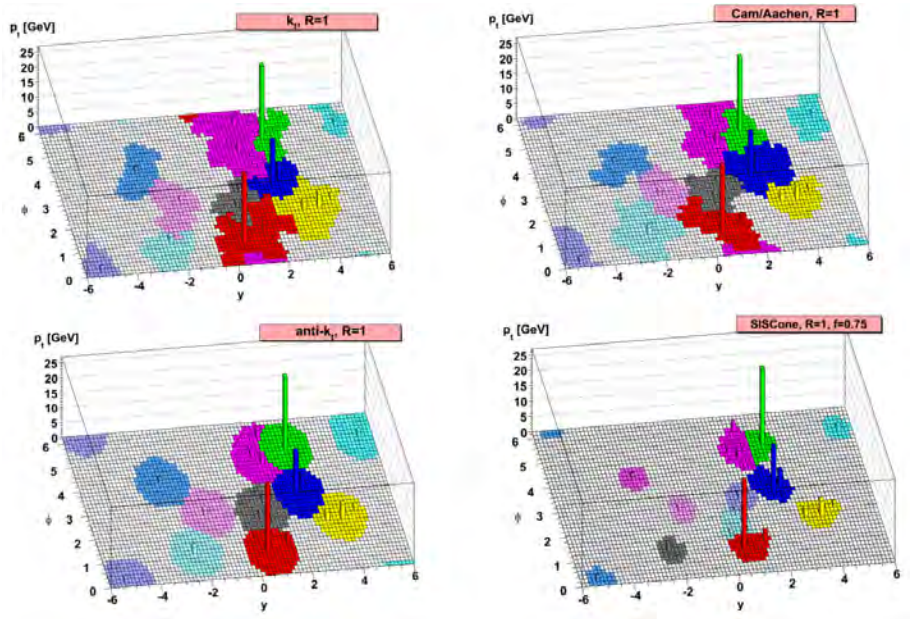

Figure 2.3: Jet shape comparison of various reconstruction algorithms. In all four cases the simulated event is exactly the same, only the jets are result of using various jet reconstruction algorithms with same jet resolution parameter $R = 1$, namely: k_T, Cambridge-Aachen, anti-k_T and SISCone. Taken from [26].

If the $d_{min} = d_{ij}$, the particles i and j are merged, removed from the list of all particles and replaced with new particle coming from merging i, j according to the given recombination scheme. Otherwise, if $d_{min} = d_i$ then the particle i cannot longer be merged and is therefore removed from the list and identified as a final jet. Then the new values of d_i and d_{ij} are calculated. This process is repeated until the list of particles is empty. Also, since the particle assigned to the particular jet is removed from the list and therefore no longer available, the complicated situation similar to the overlapping cones is not possible.

Various algorithms may differ in the condition of termination. The alternative to the one mentioned above is comparing d_{min} with a specific d_{cut}. When the $d_{cut} > d_{min}$ the merging procedure is finished. Additionally, for the proper application of the sequential jet finding algorithm, the choice of the recombination scheme is required.

2.2.1 k_T algorithm

As can be seen from Eq. (2.1), the k_T algorithm merges the closest particles with smaller p_T first, which reflects the QCD splitting [27]. Probably the most important note to mention is the fact, that k_T algorithm is by design infrared and collinear safe.

Since the k_T algorithm starts clustering the softer particles first, it is quite sensitive to the underlying background. Due to this property, it is mostly used for the estimation of jet background density, which is then used for the jet energy/momentum correction.

In addition, since the k_T algorithm works with almost every particle during the clustering process, it is quite demanding regarding the CPU time, but it is still faster than seedless cone algorithms. The algorithmic complexity of the first k_T algorithm was scaled as N^3, where N is total number of initial pre-clusters. This fact would have been an critical obstacle to the typical multiplicities achieved in collisions at the LHC energies. Luckily, the implementation of `FastJet` k_T jet finder algorithm [28] improves the complexity to

the scale of $N \ln N$, which makes it the fastest jet finder available for $N \geq 10^4$ [29] as illustrated in Fig. 2.4.

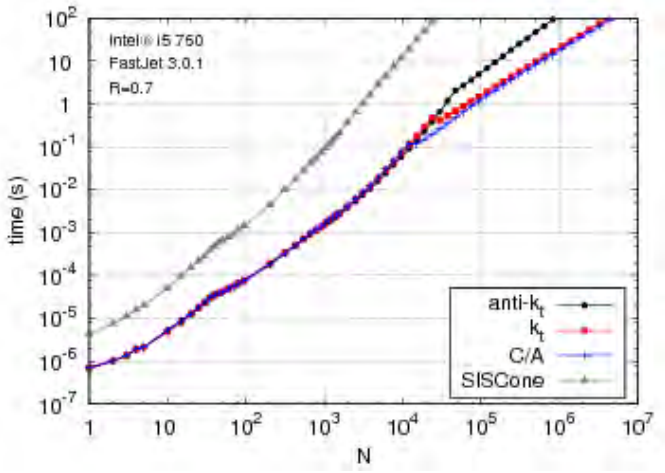

Figure 2.4: CPU time consumption as a function of number of initial particles N for various jet finding algorithms. Taken from [28].

2.2.2 Anti-k_T algorithm

For the k_T algorithm the particles are merged in the order of ascending p_T. But as it eventually turned out, more suitable choice is $p = -1$. The latter is known as the anti-k_T algorithm [26], which clusters the particles from the hardest to the softer ones.

This method naively reflects the idea of the fragmentation, where initially hard parton radiates the ones with smaller p_T. This may be interpreted as going reverse in time from the final state hadrons registered in the detector to the initial partons created during the very early phase of the collision.

Nowadays, the anti-k_T algorithm is the most commonly used jet finder for reconstruction of physical jets in all collisional system due to its well-suited properties, most importantly the relatively low sensitivity to background consisting of low-p_T particles.

2.2.3 Cambridge-Aachen algorithm

Since the d_{ij} parameter is no longer dependent on p_T when $p = 0$, the Cambridge-Aachen jet finding algorithm reconstructs jets only on the basis of the pre-cluster angular distribution. It clusters the pairs with the smallest angle first, but also provides a lower limit, when the clustering of the small-angle jet pair is no longer possible, if one of the jets is too soft [30].

Chapter 3

Baryon anomaly

The enhancement of baryon-meson ratio of protons and pions, light flavour hadrons containing only the u and d quarks, was observed in the most central heavy-ion collision at RHIC [2, 31] as illustrated in Fig. 3.1. This phenomenon referred to as baryon anomaly was later observed also for strange Λ and K^0_S hadrons at RHIC [3] and the LHC [4]. The latter is shown in Fig. 3.2. In central heavy-ion collisions the baryon-meson ratio increases with p_T and reaches its maximum around p_T of approximately 3–4 GeV/c, which is about three times larger with respect to its pp value. Then it decreases to approach the pp measurements in the region of high p_T.

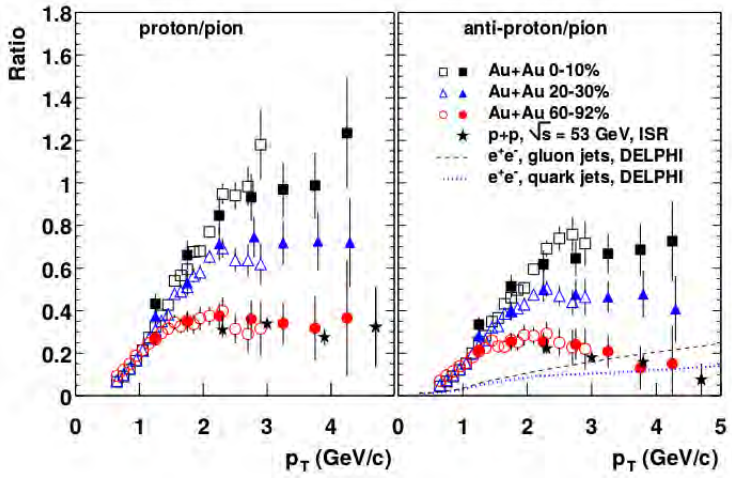

Figure 3.1: Ratio of the inclusive p_T spectra of protons and pions (left) and anti-protons and pions (right) illustrating the enhancement of baryon production in the most central Au–Au collisions with respect to the peripheral Au–Au or pp collisions measured by PHENIX experiment at RHIC. Taken from [31].

Various studies are therefore nowadays focusing on the neutral strange particle production in order to bring additional insights into the still not understood origin of the discussed baryon anomaly with an aim to disentangle the interplay of different production mechanisms listed below.

The parton fragmentation and following hadronisation is a well-known mechanism of the perturbative theory of Quantum Chromodynamics (QCD). In hard scattering processes occurring in the very early stages of the collision, a high-p_T parton is created, then it fragments and subsequently hadronises into a number of collimated softer particles (softer in a sense of smaller p_T). However, the fragmentation in the QCD vacuum alone cannot explain this anomaly. In a strongly interacting medium, such as the QGP, the parton fragmentation may be however modified due to the interactions with its constituents, i.e. the deconfined quarks and gluons.

The parton recombination is a phenomenon, which assumes that three quarks or a quark/anti-quark pair located in the densely populated phase-space cluster together and create a baryon or meson respectively [6]. In addition, due to the steeply falling parton p_T

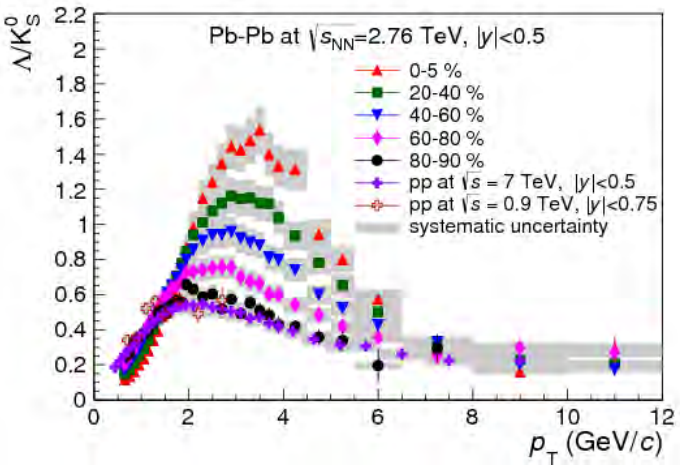

Figure 3.2: Ratio of the inclusive p_{T} spectra of neutral strange Λ baryons and $\mathrm{K}^0_{\mathrm{S}}$ mesons illustrating the enhancement of baryon production with respect to the meson production in Pb-Pb relative to the pp collisions at the LHC energy for different centrality classes measured by ALICE experiment. Taken from [4].

spectrum in the recombination picture a creation of baryons over mesons is favoured leading to enhanced baryon over meson production. This process is possible up to the hadron momentum of a few GeV/c, then its probability quickly drops and the fragmentation dominates.

Collective effects such as the radial flow may also influence the baryon-meson ratio, due to the fact that heavier particles are pushed towards higher p_{T}, which supports, by similar arguments, baryon enhancement in the region of higher momentum. A study of the radial flow ordering with respect to the strange content of the particles may bring additional insights to the studied topic [32].

In the following sections, two methods of studying the hadron production mechanisms related to the the origin of baryon anomaly of neutral strange particles are briefly introduced: the two-particle angular correlations and the hadron identification in jets.

3.1 Baryon-meson ratio from two-particle correlations

The basic concept of the two-particle angular correlation analysis based on a statistical approach is the following. Among all reconstructed particles passing certain reconstruction quality requirements and selection criteria, the particles with a high momentum in a given event are found. These are referred to as the trigger particles. From the rest of the event, the so-called associated particles of interest are selected. In the particular case of $\mathrm{h}^{\pm}$-V^0 correlation described in this section, the trigger particles are charged hadrons and the associated ones are $\mathrm{K}^0_{\mathrm{S}}$ and Λ particles, respectively.

Then for each pair of a trigger and an associated particle, the distance between trigger and associated particles in azimuth ($\Delta\varphi$) and pseudorapidity ($\Delta\eta$) is calculated. The resulting distribution has to be properly corrected for various effects, such as finite detector acceptance and presence of elliptic component and higher Fourier harmonics of flow [33].

Illustration of the corrected angular $\mathrm{h}^{\pm}$-V^0 correlation of $\mathrm{K}^0_{\mathrm{S}}$ particles measured by ALICE in Pb-Pb collisions at $\sqrt{s_{\mathrm{NN}}} = 2.76$ TeV is shown in Fig. 3.3. Such distribution

can be divided into various regions of interest. The peak region ($\Delta\eta \approx \Delta\varphi \approx 0$) contains the particles that are close to the trigger particle and can be related to the jet production, i.e. a fragmentation of parton created during the hard scattering [33]. On the other hand, the associated particles created in the region of high $\Delta\varphi$ or $\Delta\eta$ (bulk) represent the soft production. However, the away-side recoil jet peak structure is also present in the region of $\varphi \approx \pi$ (noted here as Bulk II). It was observed that at the intermediate transverse momenta p_{T} of 3–6 GeV/c, which are of interest for the topic of this thesis, in the central heavy-ion collisions the away-side peak disappears [34]. In order to separate the production associated with high-p_{T} particles additional assumption that the bulk production and fragmentation processes can be factorised, i.e. there is no connection between them [33].

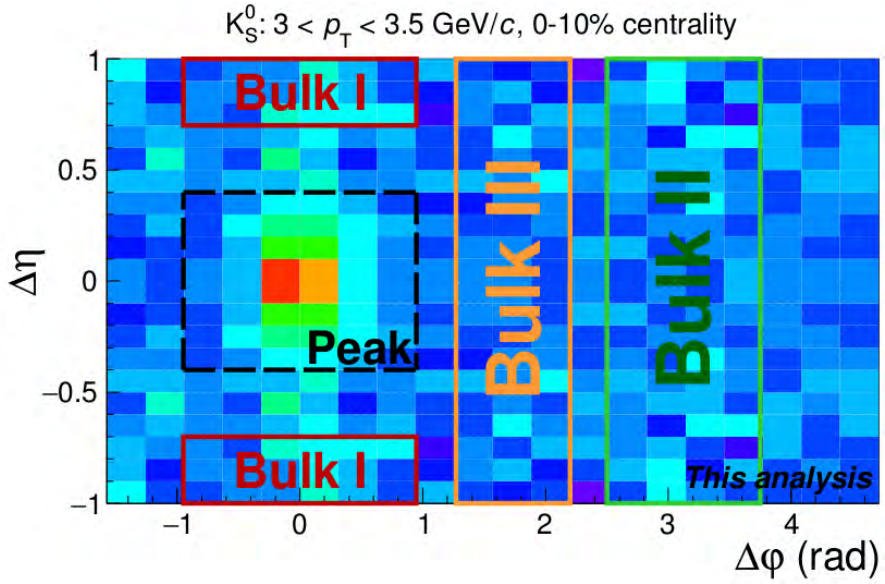

Figure 3.3: Corrected $\Delta\eta \times \Delta\varphi$ distribution of $\mathrm{h}^{\pm}$-$\mathrm{K}^0_{\mathrm{S}}$ angular correlation and definition of a near-side peak and various bulk regions used for a study of the V^0 production in Pb-Pb collisions at $\sqrt{s_{\mathrm{NN}}} = 2.76$ TeV measured by ALICE. Taken from [33].

Comparing the yields of V^0 particles detected in different $\Delta\varphi, \Delta\eta$ regions may therefore bring insights into the particle production mechanisms. The results of analysis of $\Lambda/\mathrm{K}^0_{\mathrm{S}}$ ratio in different regions of angular distribution (as illustrated in Fig. 3.3) obtained via the two-particle $\mathrm{h}^{\pm}$-V^0 correlation in Pb-Pb collisions at $\sqrt{s_{\mathrm{NN}}} = 2.76$ TeV as a function of V^0 p_{T} are presented in Fig. 3.4. When compared to the ratio of inclusively produced V^0 particles, the V^0 production in the near-side peak region, where the hard processes dominate, resembles that of the inclusive V^0 production in pp collisions. On the other hand, in the most central heavy-ion collisions the $\Lambda/\mathrm{K}^0_{\mathrm{S}}$ ratio is similar to the bulk region and thus dominated by the soft processes.

Therefore, the results of the $\mathrm{h}^{\pm}$-V^0 correlation study indicate that the observed enhancement in baryon-meson ratio might be related to the hadronisation of the hot and dense medium, which is expected to be not present in small systems [33].

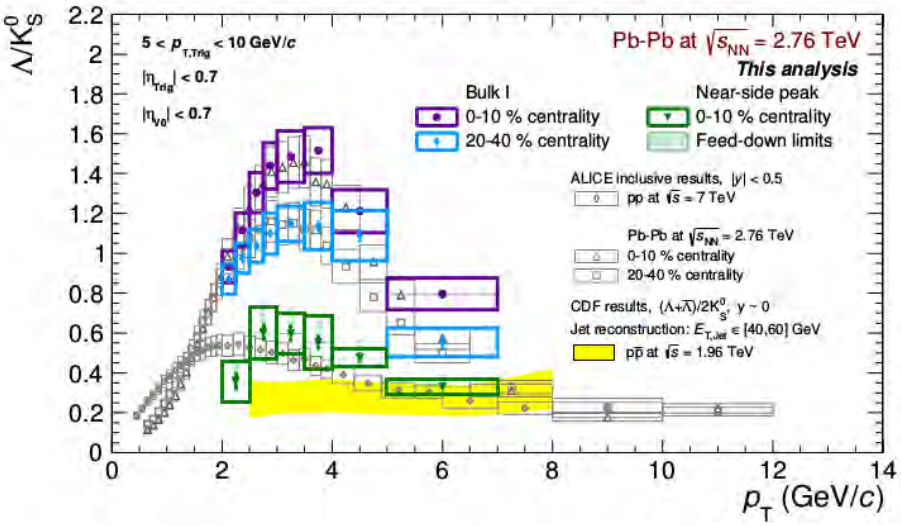

Figure 3.4: Ratio of the Λ and K^0_S particles produced in the near-side peak (solid triangles) and the bulk regions (solid circles and diamonds) obtained via the $h^{\pm}$-V^0 angular correlation as a function of V^0 p_T for two centrality classes of Pb-Pb collisions at $\sqrt{s_{NN}} = 2.76$ TeV. The open symbols represents the results of inclusively produced V^0 particles in Pb-Pb at $\sqrt{s_{NN}} = 2.76$ TeV and pp at $\sqrt{s} = 7$ TeV collisions. Taken from [33].

3.2 Baryon-meson ratio of particles produced in jets

With respect to the statistical approach described in previous section, the hadron identification in jets allows more direct access to information about the hard scattering processes occuring during the collisions.

Since the hadron identification is the main topic of this thesis, the latest results of the analysis of V^0 production associated with the jets will be presented in this section and the description of the methodology itself will be in detail discussed in Chapter 5.

The neutral strange baryon-meson ratio of the V^0 particles associated with the charged jets produced in the most central Pb-Pb collisions at $\sqrt{s_{NN}} = 2.76$ TeV altogether with the published inclusive results [35,36] measured by ALICE experiments is presented in Fig. 3.5. As can be seen, the baryon-meson ratio of V^0 particles associated with jets is much smaller than the inclusive production in the region of intermediate p_T. That indicates that the inclusive V^0 production is dominated by the soft processes. The results is also not very sensitive to the jet selection in a form of minimum jet p_T criterion within the statistical uncertainty.

The results for the high-multiplicity p-Pb collisions at $\sqrt{s_{NN}} = 5.02$ TeV [37], where only cold nuclear matter effects are expected, are shown in Fig. 3.6. Apart from the V^0 and jet p_T dependency, it also illustrates a negligible dependency on the jet resolution parameter R. The baryon-meson ratio of V^0 associated with jets exhibits similar behaviour as the PYTHIA predictions in p-Pb collisions.

When compared to the inclusive V^0 production shown in Fig. 3.2, both results exhibit a similar behaviour and magnitude as the results from pp collisions. This observation is compatible with the results of the previously discussed correlation study. However, for the proper understanding of the baryon anomaly phenomenon, the analysis of V^0 associated with jets in pp collisions is essential.

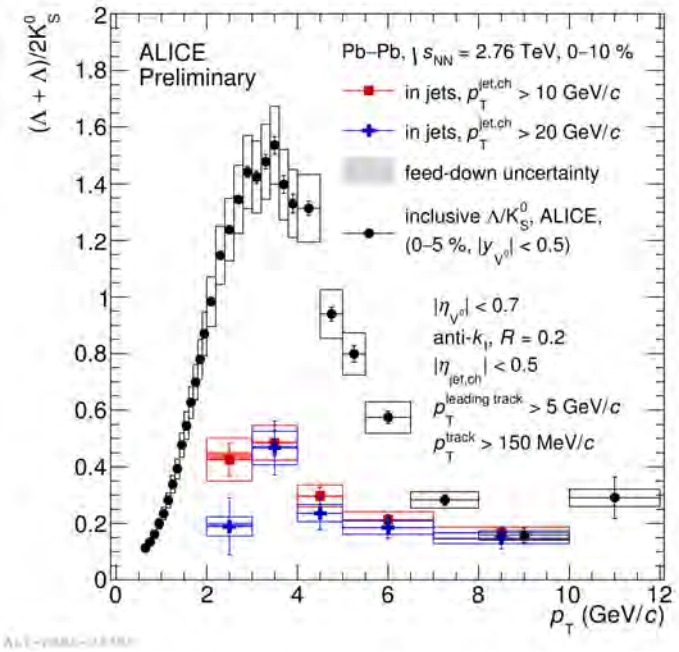

Figure 3.5: Ratio of $\Lambda/\bar{\Lambda}$ and K^0_S associated with the charged jets with two values of the minimum jet p_T selection criterion (color) and the inclusive ratio (black) in the most central Pb-Pb collisions at $\sqrt{s_{NN}} = 2.76$ TeV. Taken from [35, 36].

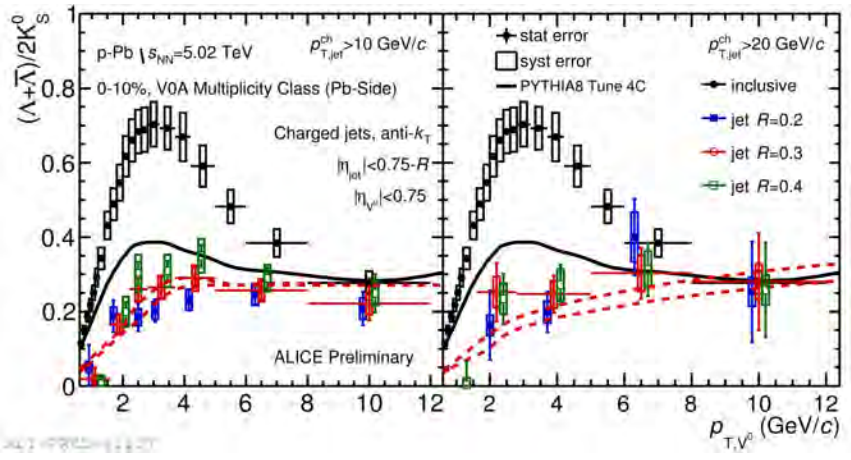

Figure 3.6: Ratio of $\Lambda/\bar{\Lambda}$ and K^0_S associated with the charged jets with the minimum jet p_T selection criterion: 10 GeV/c (left), 20 GeV/c (right); three values of jet resolution parameters (color) and the inclusive ratio (black) in the high multiplicity p-Pb collisions at $\sqrt{s_{NN}} = 5.02$ TeV. The black solid line represents the inclusive ratio from the `PYTHIA` simulation and the red dashed lines represents the ratio of V^0 in MC jets. Taken from [37].

Chapter 4

ALICE

ALICE (A Large Ion Collider Experiment) is one of the four large experiments at the LHC at CERN and the only experiment dedicated to study the ultra-relativistic heavy-ion collisions. ALICE is therefore optimized for extremely high multiplicities and designed to be complementary to the other LHC experiments, namely ATLAS, CMS and LHCb.

ALICE is a multi-purpose detector consisting of a total number of 18 various detecting sub-systems distributed among the two main parts: central barrel detectors or forward muon spectrometer.

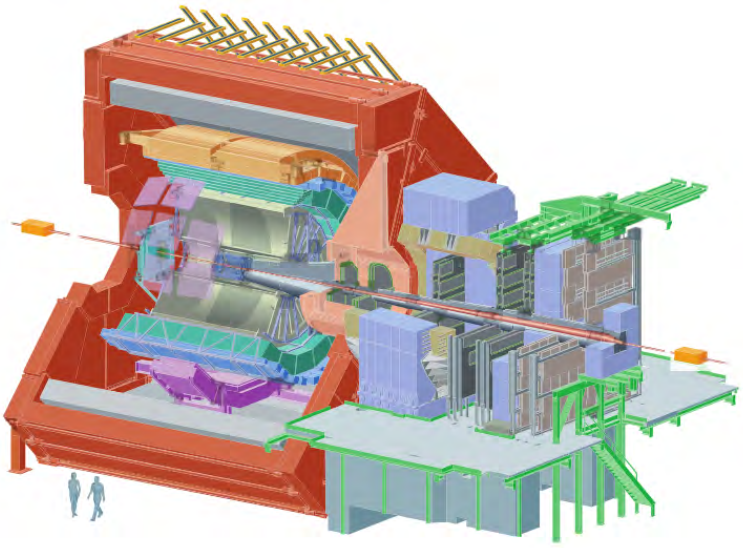

Figure 4.1: Schematic illustration of the ALICE detector. Taken from [38].

Forward muon spectrometer, as the name suggests, contains detectors for measuring $\mu^{\pm}$ coming from the leptonic decays of ϕ mesons or heavy-flavour quarkonia (bound states of $q\bar{q}$ pairs of the same flavour), such as J/ψ or Υ.

Central barrel detectors, covering polar angle region from 45° to 135° (corresponding to approximate pseudorapidity coverage of $|\eta| \leq 0.9$) and full azimuth, are embedded in a large solenoidal magnet with nominal magnetic field of 0.5 T from the superseded L3 experiment at LEP (Large Electron Positron collider). The main purpose of this detector system is tracking and particle identification (PID) of hadrons, electrons and photons.

In following sections, only detection systems that are particularly relevant to the discussed analysis of neutral strange particles production in jets or to jet analysis in general are described. A more detailed description of the whole ALICE detector and its sub-systems can be found in [38].

4.1 Inner Tracking System

The main tasks of the Inner Tracking System (ITS) are the localization of a primary vertex (PV) or an interaction point, the point along the beam direction z-axis, where the collision occurs; and the reconstruction of secondary vertices of heavy-flavour hadrons, such as D and B mesons and hyperons decays (particles containing at least one strange quark, e.g. Λ). The ITS is also capable of tracking and PID of hadrons with p_{T} from 200 MeV/c and therefore improves the tracking resolution and overall possibilities of main tracking detector of ALICE experiment, the Time-Projection Chamber.

The ITS consists of three pairs of the cylindrical layers of silicon detectors surrounding the beryllium beam pipe and thus it is the closest detector with respect to the primary vertex with transverse distance ranging from 4 to 43 cm. First two layers are the Silicon Pixel Detectors (SPD) chosen carefully in order to fulfil the requirements for the high precision of primary vertex localisation and high particle density. Then follows the two layers of Silicon Drift Detectors (SDD) and two outer layers consists Silicon Strip Detectors (SSD).

Contrary to the SPD, these four outer layers are equipped with an analogue readout chip, allowing to estimate the characteristic $\mathrm{d}E/\mathrm{d}x$ ionization losses of non-relativistic low momentum particles. The material budget of the ITS is very low, $\approx 5\%$ of radiation length X_0.

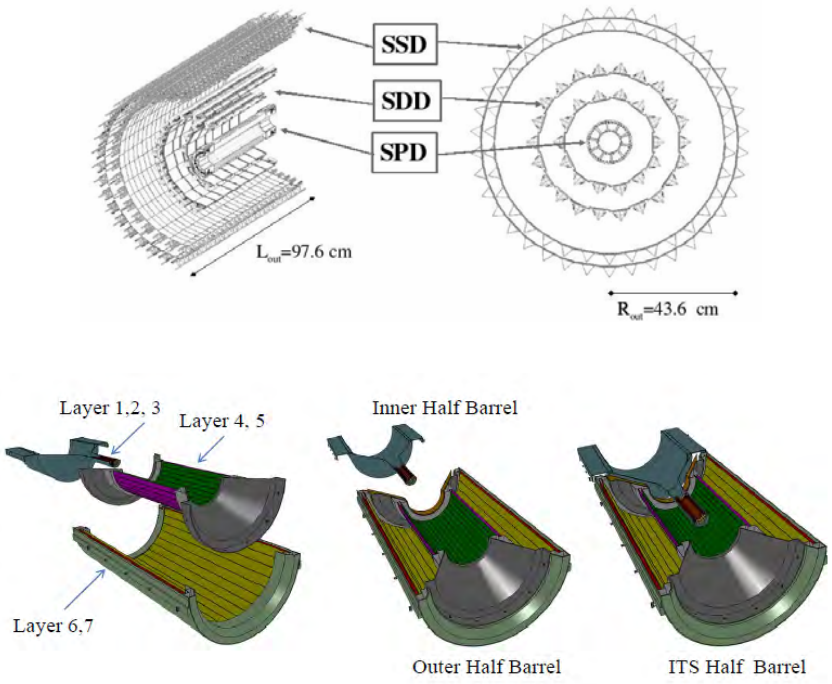

Figure 4.2: Schematic illustration and radial cross-section of Inner Tracking System consisting of three pairs of silicon pixel detectors.

4.2 Time Projection Chamber

The Time Projection Chamber (TPC) provide the unique capabilities both for the tracking and the particle identification. It is used as a main tracking detector in the central barrel providing up to 159 space-points per track with good two-track separation and momentum resolution in wide range of p_{T} ranging from 0.1 GeV/c up to 100 GeV/c. The TPC is capable of proton, kaon, pion and electron identification up to order of tens of GeV/c with good particle identification separation.

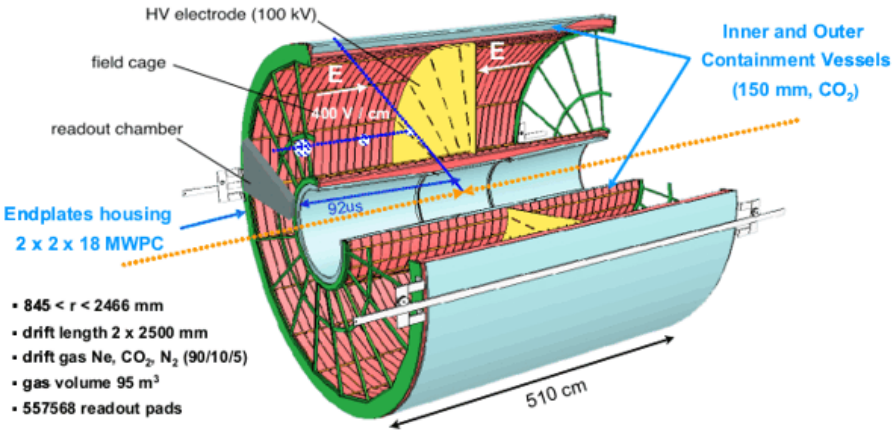

Figure 4.3: Schema and technical specifications of the ALICE Time-Projection Chamber.

By design, the TPC is a cylindrical drift detector with multi-wire proportional chambers on each side and overall pseudorapidity coverage of $|\eta| \leq 0.9$ consisting of field cage with dimensions of 500 cm in beam direction and inner and outer radii of 85 and 247 cm, respectively, filled with approximately 90 m^3 of $\mathrm{Ne/CO_2/N_2}$ mixture.

The TPC was designed to fully withstand the huge particle densities, which were first estimated by extrapolating the RHIC data to the LHC energies [38]. The TPC should be able to cope with than 20 000 charged particles (both primary and secondary) inside its sensitive volume. In case of Pb-Pb collisions, the TPC was designed to operate with a frequency of 200 Hz, making the TPC the "slowest" sub-system of ALICE. This disadvantage is one of the important tasks discussed for future upgrades of the ALICE detector.

4.3 Time-of-Flight detector

In addition to the TPC, the Time-of-Flight (TOF) detector is used for the particle identification of pions and kaons up to 2.5 GeV/c, and protons with maximal momentum of 4 GeV/c. It also provides good K/π and K/p separation.

The TOF detector is a 141 m^2 cylindrical array of gaseous Multi-gap Resistive Plate Chambers situated at radial distance of 370 cm to the beam pipe with coverage $|\eta| \leq 0.9$ in pseudorapidity and full in azimuth except a relatively small area in front of the Photon Spectrometer due to the material reduction.

Time-of-flight particle identification method is based on a proper estimation of the time interval between the collision and the moment when a particle arrives to the TOF detector

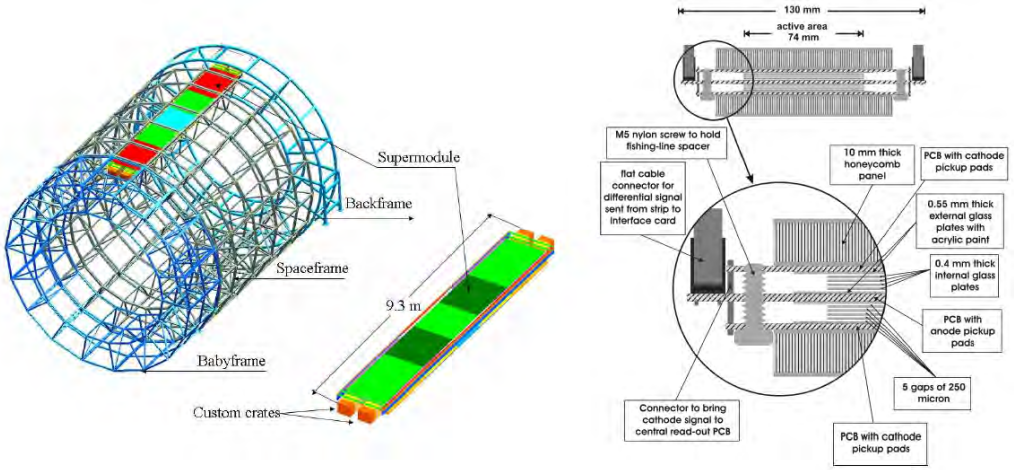

Figure 4.4: Schema of the ALICE TOF detector (left hand side) and specifications of its module (right hand side).

(arrival time). Since the distance from the interaction point to the TOF is well-defined, with this information, one can estimate the velocity of the measured particle. Additionally, if the particle momentum is known, the mass can be derived and therefore one can identify the detected particles.

The starting time is estimated via a T0 detector, which is a pair of Cherenkov counters located near the beam pipe opposite to each other with centre of the ITS in between them. Besides the time to the TOF detector, it provides information about the primary vertex position and is also used as the lowest level (L0) trigger.

4.4 Electromagnetic Calorimeter

Since most of the detecting systems mentioned in previous sections operate only with the charged particles, the need for a detector of electrically neutral particles have arisen, especially in the field of jet studies, where the fragmentation processes may lead to the creation of relatively large number of neutral and thus undetectable particles. Consequently, one has to choose whether to reconstruct the charged jets, where information based only on detector response to the charged particles is used; or the full jets including also the information about neutral part of the hadronic content of the jets. The latter was made possible by including an Electromagnetic Calorimeter (EMCal) among the ALICE detectors.

The EMCal is a Pb-scintillator sampling calorimeter located 4.5 m from the beam pipe with overall acceptance of $|\eta| \leq 0.7$ in pseudorapidity and 107° in azimuth. This limited coverage with respect to the other detecting sub-systems is due to the lack of free space available inside the L3 coil and the fact that the EMCal was not considered from the very beginning of the ALICE design, but added later in order to address the question of jet quenching phenomena (discussed in section 1.5).

Implementation of a new Di-jet Calorimeter (DCal) detector for the LHC Run 2 in the region opposite to the EMCal will significantly improve the current situation about the calorimetry capabilities of ALICE detector [39]. The addition of the DCal allows more precise measurement of jets spectra as well as more detailed study of physically interesting phenomena such the di-jets (two jets originating in the same spot but propagating in almost opposite directions) or hadron-jet correlations.

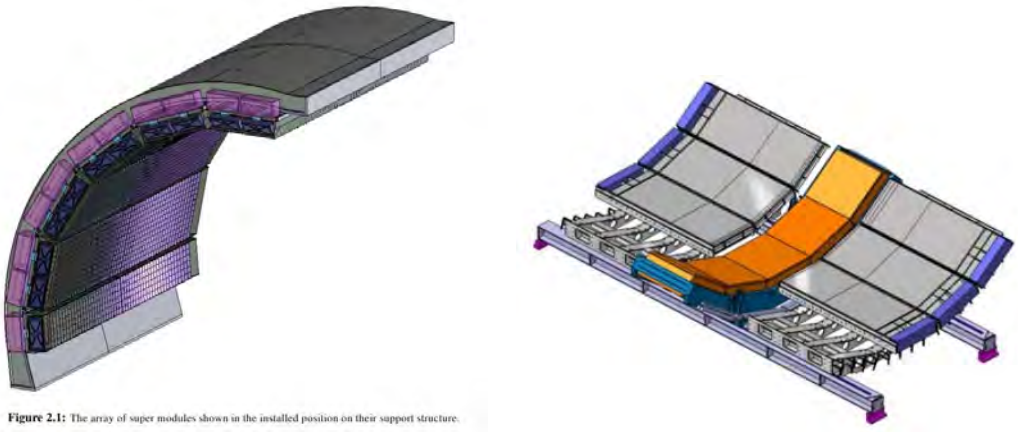

Figure 4.5: Schematic illustration of the EMCal (left hand side) and the newly installed DCal (right hand side). Taken from [39].

Chapter 5

Analysis of neutral strange particles production

In this chapter, the detailed description of the analysis of K^0_S, Λ and $\overline{\Lambda}$ particles produced inclusively as well as associated with charged jets in proton-proton collisions at $\sqrt{s} = 7$ TeV recorded with the ALICE detector is presented. These neutral strange particles are generally referred to as the V^0 particles due to their characteristic two-body decay topology discussed in more detail in Sec. 5.3.

For the purpose of the analysis `AliROOT` software, the extension to the scientific data analysis framework `ROOT` [40], developed specifically for the purposes of the ALICE Collaboration is used. This environment created at CERN and based on `C++` language is used for a statistical processing of large data samples, their storage and visualization. `AliROOT` includes additional libraries such as `AliPhysics` package containing all code necessary for processing of data produced by the ALICE. The backbone of any ALICE analysis is the class `AliAnalysisTask` which implements basic methods and properties on which all specific analyses are based.

The analysis is conducted using the class `AliAnalysisTaskV0sInJetsEmcal` available in `AliPhysics` package, which results are then further processed. All consecutive steps of the analysis chain discussed in the following sections are listed below and schematically illustrated in Fig. 5.1:

1. Event selection
2. Topological reconstruction of the inclusive V^0 candidates
3. Inclusive jet reconstruction
4. V^0-jet matching procedure
5. Inclusive and in-jet yield of V^0s estimation via the signal extraction
6. Correction application
7. Spectra and baryon-meson ratio processing

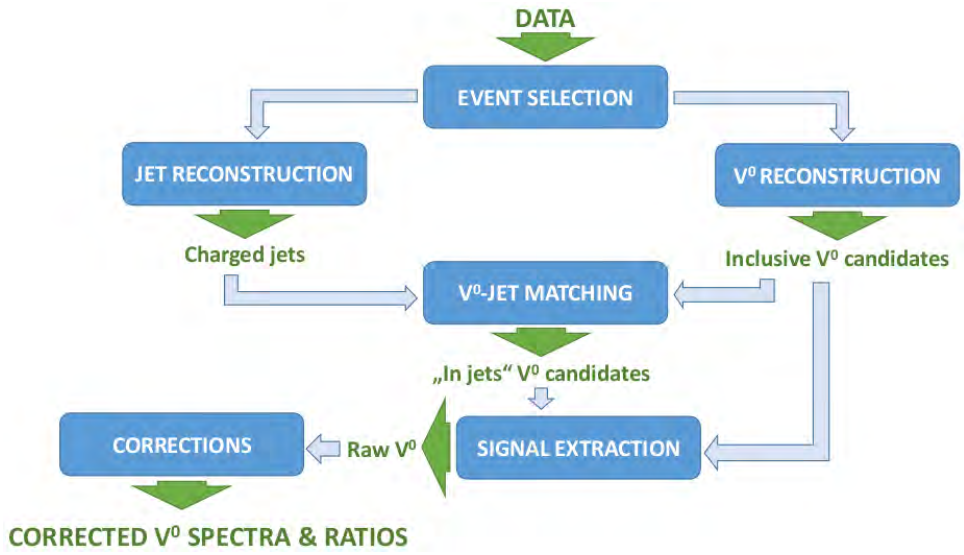

Figure 5.1: The diagram of consecutive steps of analysis of inclusive V^0 as well as V^0 production associated with the charged jets.

5.1 Data sample

For analysis presented in this thesis the data from the proton-proton (pp) collisions at the centre-of-mass energy $\sqrt{s} = 7$ TeV taken in the LHC Run 1 by the ALICE detector in the year 2010 have been used. Specifically, datasets from the `pass2`[1] reconstruction cycle of LHC10d period listed in the good run list LHC10d_AOD135 with flat azimuthal angle ϕ distribution. Such requirement is essential for a proper jet study, otherwise any larger inhomogeneity in the track $\eta \times \phi$ distribution, where η is the pseudorapidity, may introduce a bias to the reconstructed jet sample. This good run list is commonly used for various jet related studies in pp collisions within the ALICE Physics Working Group Jets (PWG-JE).

Run numbers included in the LHC10d_AOD135 are the following: 122374, 125023, 125085, 125097, 125100, 125101, 125134, 125139, 125140, 125156, 125186, 125296, 125630, 125632, 125633, 125842, 125843, 125844, 125847, 125848, 125849, 125850, 125851, 125855, 126004, 126007, 126008, 126073, 126078, 126081, 126082, 126088, 126090, 126097, 126158, 126284, 126285, 126351, 126352, 126359, 126403, 126404, 126405, 126406, 126407, 126408, 126409, 126422, 126424, 126425, 126432, 126437.

Before applying any selection criteria or additional quality requirements the data sample consisting of runs listed above contains more than 140 million events.

5.2 Event selection

Only the minimum bias (MB) events tagged as `AliVEvent::kMB` passing additional conditions concerning the event selection and the primary vertex (PV) have been used:

- excluding the pile-up event via `AliAODEvent::IsPileUpFromSPD()`,
- at least 3 contributors to the PV,

[1] The pass generally corresponds to a given iteration of offline data reconstruction procedure which is applied when certain improvements is achieved, for instance after implementing improved algorithm for track reconstruction.

- maximal z distance between PV and interaction point of 10 cm,
- radial distance r from beam axis smaller than 1 cm,
- reconstructed from SPD and TPC, but not based only on TPC.

After applying all the selection criteria listed above, the data sample used in this analysis contained approximately 100 million events.

5.3 V^0 candidate reconstruction

The neutral strange K^0_S, Λ and $\overline{\Lambda}$ particles decay via the weak interaction into a pair of daughter particles with opposite charge (see Table 5.1). In a presence of a homogeneous external magnetic field, two daughter particles travel in such directions that the characteristic "V-shaped" decay geometry is observed. K^0_S and $\Lambda/\ \overline{\Lambda}$ particles are therefore referred to as V^0 for their neutral electric charge and characteristic "V-shaped" decay topology illustrated in Fig. 5.2, which can be described by the following several parameters:

- **Distance of Closest Approach (DCA) of daughter tracks**
  Minimal distance between the two daughter tracks
- **Primary vertex (PV)**
  Point, where the collision occurs
- **Secondary vertex (SV)**
  Point defined in the middle of the daughter track DCA
- **DCA to the PV**
  Minimal distance between the daughter tracks and the primary vertex
- **Decay radial length**
  Distance between the primary vertex and the secondary vertex
- **Cosine of pointing angle (CPA)**
  Cosine of the angle between the PV and the SV line and reconstructed V^0 momentum

Decay channel	BR [%]	m^{mother} [MeV/c^2]	τ^{mother} [ps]
$K^0_S \longrightarrow \pi^+ + \pi^-$	69.2	497.61 ± 0.013	89.56 ± 0.04
$\Lambda \longrightarrow p + \pi^-$	63.9	1115.683 ± 0.006	263 ± 2
$\overline{\Lambda} \longrightarrow \overline{p} + \pi^+$	63.9	1115.683 ± 0.006	263 ± 2

Table 5.1: V^0 decay channels characteristics of K^0_S, Λ and $\overline{\Lambda}$ particles, the branching ratio BR, the mass of the mother particle m^{mother} and its mean lifetime τ^{mother} [41].

The V^0 candidate selection was conducted by an offline method based on the various topological criteria and kinematic cuts in order to suppress as much combinatorial background as possible without loosing too many signal particles. Values of these cuts were chosen to be in agreement with the analysis of the inclusive K^0_S and $\Lambda/\ \overline{\Lambda}$ production in pp collisions performed in the Physics Working Group Light Flavour (PWG-LF) [43]. The complete list of cuts and selection criteria is presented in Table 5.2.

First, the standard quality cuts for charged V^0 candidate daughter tracks were applied, such as a minimum value of the number of crossed TPC rows over number of findable TPC clusters ratio. In addition, the TPC refit was done and kink tracks were rejected. If one

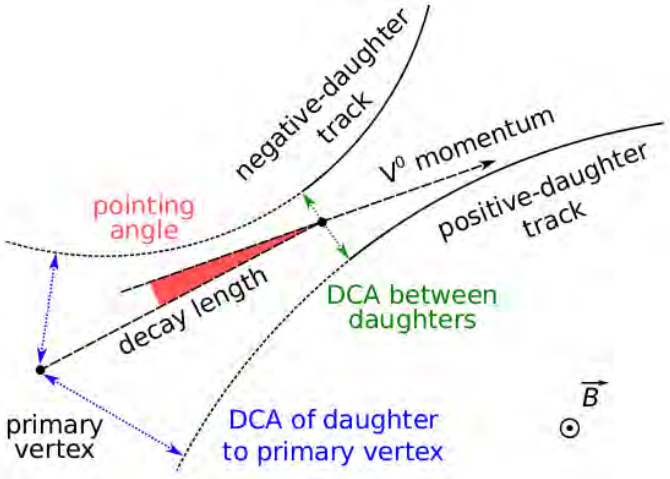

Figure 5.2: Characteristic topology of a neutral strange particle decay together with an illustration of the meaning of various V^0 topological reconstruction parameters [42].

Parameter	Value
Track TPC refit	`AliAODTrack::kTPCrefit`
Vertex tracks type	`!AliAODVertex::kKink`
Number of findable TPC clusters	> 0
Number of crossed TPC rows	≥ 70
Crossed TPC rows over findable clusters	≥ 0.8
Daughter DCA to PV	≥ 0.06 cm
DCA between daughters	$\leq 1\sigma$ (TPC tracking)
CPA (K^0_S)	≥ 0.97
CPA ($\Lambda/\overline{\Lambda}$)	≥ 0.995
Decay radial length	$0.5 \leq r \leq 100$ cm
Track pseudorapidity	$\lvert\eta^{\text{track}}\rvert \leq 0.8$
V^0 pseudorapidity	$\lvert\eta^{\text{V0}}\rvert \leq 0.7$
Proper life-time (K^0_S)	$\leq 7.45\ c\tau$
Proper life-time ($\Lambda/\overline{\Lambda}$)	$\leq 3.8\ c\tau$
Armenteros-Podolanski cut(K^0_S)	$p_{\text{T}}^{\text{Arm}} \geq 0.2\lvert\alpha\rvert$
Cross-contamination rejection (K^0_S)	$\lvert M_{\Lambda}^{\text{V0}} - M_{\Lambda}^{\text{PDG}}\rvert < 5$ MeV/c^2
Cross-contamination rejection ($\Lambda/\overline{\Lambda}$)	$\lvert M_{K^0_S}^{\text{V0}} - M_{K^0_S}^{\text{PDG}}\rvert < 10$ MeV/c^2

Table 5.2: Selection cuts and criteria for daughter tracks and inclusive V^0 candidates.

of the particles from two-body decays cannot be detected (e.g. weak decays of charged kaons), the other track appears to be bended with no reason. These tracks, referred to as kink tracks, are often not precisely reconstructed due to split-merging procedure.

Then the topological cuts listed above were applied. In this analysis particle identification (PID) of V^0 daughters via the TPC dE/dx information was not applied, since it has no significant effect for particles with $p_T > 2$ GeV/c [42].

Finally, the pseudorapidity cut on reconstructed V^0 candidates and the particle dependent criteria was applied for a proper life-time in the transverse plane[2] and the Armenteros-Podolanski α variable[3] as illustrated in Fig. 5.3.

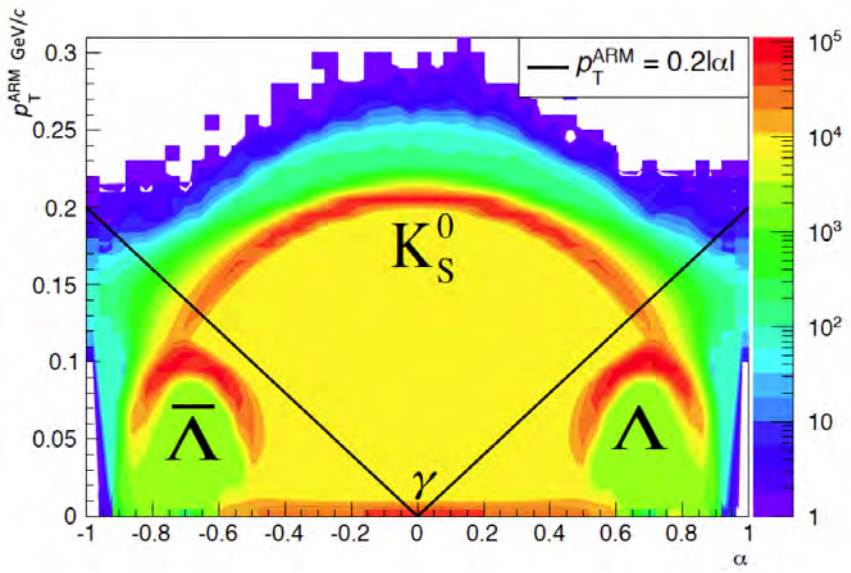

Figure 5.3: The illustration of Armenteros-Podolaski plot used for distinguishing the V^0 particles. Solid lines represents the used boundaries of the regions, where V^0 are identified. Taken from [33].

5.4 Jet reconstruction

For estimation of strange particle production associated with jets, jet reconstruction is needed. Since the jet reconstruction is done in parallel to the V^0 finding, resulting inclusive jets are therefore independent of V^0 reconstruction procedure.

In the analysis presented here, only the charged jets were reconstructed, meaning that tracks of charged particles passing selection criteria listed below were clustered with no additional information from the electromagnetic calorimeter about the electrically neutral part of the parton shower. This is due to the rather small acceptance of the EMCal detector, which would result to additional loss of jet sample, which is already limited. In addition the tracks used for jet reconstruction had to fulfil certain detection quality criteria, commonly used within the PWG-JE, referred to as "hybrid tracks" (specially selected sample of tracks in order to obtain the already discussed flat distribution in ϕ space)w. Overall, the charged tracks have to meet the following criteria:

[2]Estimated as $c\tau = \frac{rmc^2}{p_T c}$, where r is the decay radius in $x \times y$ plane.

[3]Given by $\alpha = \frac{q_L^+ - q_L^-}{q_L^+ + q_L^-}$, where $g_L^{+/-}$ is a longitudinal momentum of positively/negatively charged daughter with respect to the mother total momentum.

- Tagged as a "hybrid track"
- Minimum track p_{T} of 150 MeV/c
- Pseudorapidity range in detector acceptance $|\eta^{\mathrm{track}}| < 0.9$

Tracks passing listed requirements serve as an input for the jet reconstruction algorithm carried by the sequential recombination anti-k_{T} algorithm from the `FastJet` package [44] and implemented in the `AliPhysics` class `AliEmcalJetTask` with the following parameters.

- Jet resolution parameter $R = 0.3$ (0.2, 0.4)
- Charged jets
- p_{T} recombination scheme

After the jet-finding procedure additional selection criteria listed below were applied in order to suppress the combinatorial (or "fake") jets and increase the probability of selecting the hard-scattering processes.

- Minimum jet p_{T} of 8 GeV/c (5 GeV/c, 10 GeV/c)
- Minimum jet area $A = 0.6\pi R^2$
- Full jet inside the pseudorapidity acceptance of V^0 $|\eta^{\mathrm{jet}}| < |\eta^{\mathrm{V}^0}| - R$

The values in parentheses have been used for studying the result dependency on given parameters. For the proper interpretation of comparison between inclusive V^0 production and production of identified V^0 associated with jet, the additional condition that the whole jet cone is lying inside the V^0 acceptance is introduced. The parameter D is an angular distance between the V^0 momenta and the jet axis used for the purpose of V^0-jet matching procedure (see Sec. 5.5).

An uncorrected η and ϕ distributions and p_{T} spectra of reconstructed charged jets fulfilling the requirements mentioned in this section are shown in Fig. 5.4 and Fig. 5.5 respectively.

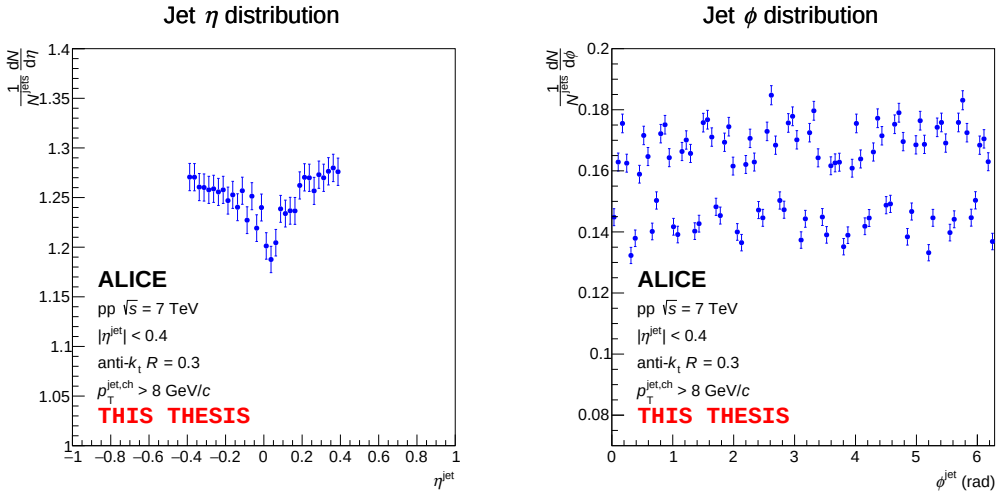

Figure 5.4: Distribution of η (left) and ϕ (right) of jets with the minimum jet $p_{\mathrm{T}}^{\mathrm{jet,ch}} > 8$ GeV/c reconstructed via the anti-k_{T} algorithm with jet resolution $R = 0.3$.

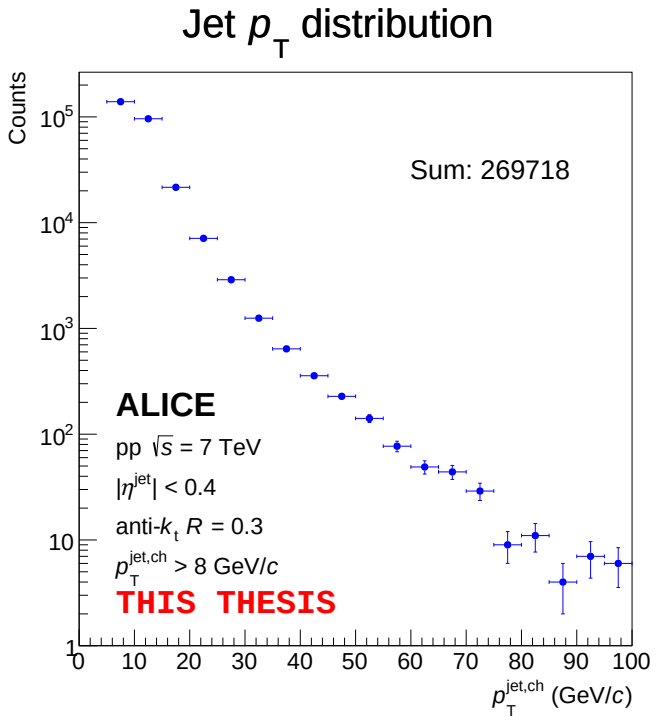

Figure 5.5: p_{T} distribution of jets with the minimum jet $p_{\mathrm{T}}^{\mathrm{jet,ch}} > 8$ GeV/c reconstructed via the anti-k_{T} algorithm with the jet resolution $R = 0.3$.

5.5 V^0-jet matching

The V^0-jet matching procedure has been done based on the geometrical basis. The only criterion for associating the V^0 candidate with the jet is following. If the distance in $\eta \times \phi$ space between the reconstructed V^0 candidate momentum and the jet axis $\Delta R = \sqrt{(\eta^{\mathrm{jet}} - \eta^{\mathrm{V}^0})^2 + (\phi^{\mathrm{jet}} - \phi^{\mathrm{V}^0})^2} \leq D$ is smaller than certain value given by the V^0-jet-matching parameter D, then the V^0 candidate is considered as associated with the particular jet (and referred to as an in-jet V^0). In this analysis, the value of D parameter was set equal to the value of the jet resolution parameter R.

5.6 Signal extraction

The reconstructed V^0 candidates have been divided into several groups based on their p_{T}, and consequently the signal particles (and their respective yield) extraction was conducted in each p_{T} interval separately by the procedure described in this section. This was done both for the inclusive V^0 candidates and also for the Monte Carlo simulated particles during the reconstruction efficiency correction estimation. In the case of V^0 candidates associated with jets the original distribution has been divided into groups based not only on p_{T} of the V^0 candidate but on its η as well, since the V^0 candidate distribution is not uniformly distributed in pseudorapidity, but instead modified according to the jet η distribution.

First, the invariant mass m_{inv} distribution of V^0 candidates is fit with a sum of Gaussian and polynomial function representing the signal and combinatorial background. From the result of this fit, the values of Gaussian distribution standard deviation σ and mean μ are extracted and used for the estimation of invariant mass limits of peak region and

background side-bands, $m^{\mathrm{P}} \in \langle \mu{-}6\sigma; \mu{+}6\sigma \rangle$ and $m^{\mathrm{SB}} \in \langle \mu{-}12\sigma; \mu{-}6\sigma \rangle \cup \langle \mu{+}6\sigma; \mu{+}12\sigma \rangle$, respectively (see Fig. 5.6).

Then the invariant mass distribution is fit with a polynomial function in the both background side-band regions simultaneously, while excluding the peak region. The degree of polynomial function was chosen in the following way. For $\mathrm{K}^0_{\mathrm{S}}$ the linear function was used. In case of Λ or $\overline{\Lambda}$ particles a cubic polynomial function was chosen due to the fact that the overall shape of the background in vicinity of the peak changes dramatically with the p_{T}. A polynomial function with lower degree than the initial is used in the given p_{T} (and η) window when the overall number of candidates is low.

The resulting yields of V^0 particles are obtained via a bin counting method in the peak region, when the number of signal particles is estimated simply as a bin content subtracted by the value of fitted background function in the bin centre. The purity P of the signal in a given p_{T} (and η) window is then defined as a ratio of signal particles and sum of signal and background particles in the peak window:

$$P(p_{\mathrm{T}}, \eta) = \frac{N^{\mathrm{signal}}(p_{\mathrm{T}}, \eta)}{N^{\mathrm{signal}}(p_{\mathrm{T}}, \eta) + N^{\mathrm{BG}}(p_{\mathrm{T}}, \eta)}\Big|_{m^{\mathrm{P}}}. \tag{5.1}$$

Since the overall number of V^0 candidates associated with jets is quite low with respect to the inclusive production and therefore the fitting procedure is more difficult, an alternative method for yield estimation is applied. Only the sum of Gaussian and polynomial function is fitted in each p_{T}–η window and the number of candidates in the peak region m^{P} is extracted (without the background subtraction). This number is then multiplied by the purity obtained from the full signal extraction procedure conducted on the inclusive V^0 candidate distribution with the same p_{T}–η binning as in the in-jet case shown in Fig. 5.7. The resulting number is then considered as the number of raw (uncorrected) signal V^0 particles associated with the jets.

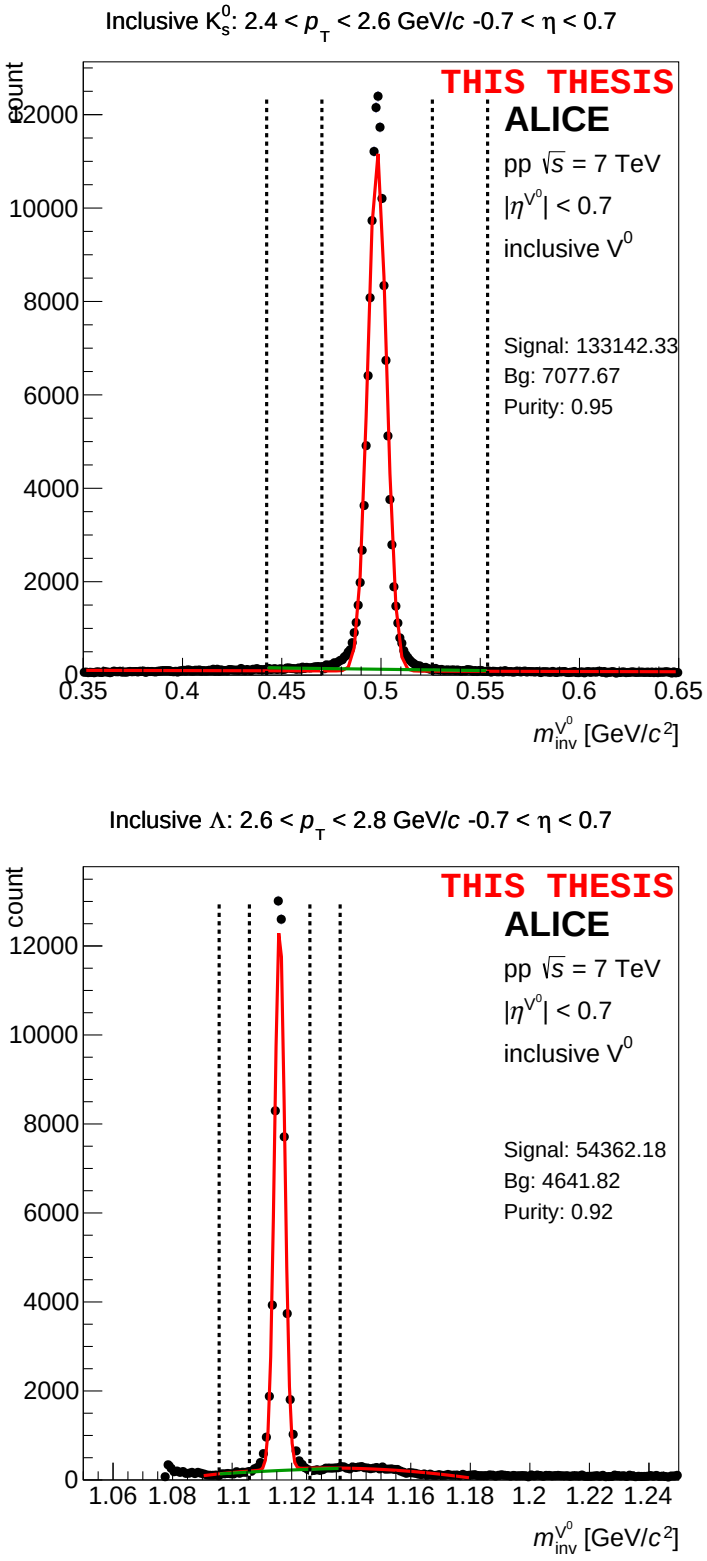

Figure 5.6: Examples of the fitting of the invariant mass distribution m_{inv} of inclusive V^0 candidates in a given p_T bin: K^0_S (top) and Λ (bottom). The red line indicates the approximative fit from which the value of μ and σ is obtained, the vertical dashed lines correspond to the $\mu \pm 12\sigma$ and $\mu \pm 6\sigma$ boundaries and the green line is the function for background estimation in the peak region m^{P}.

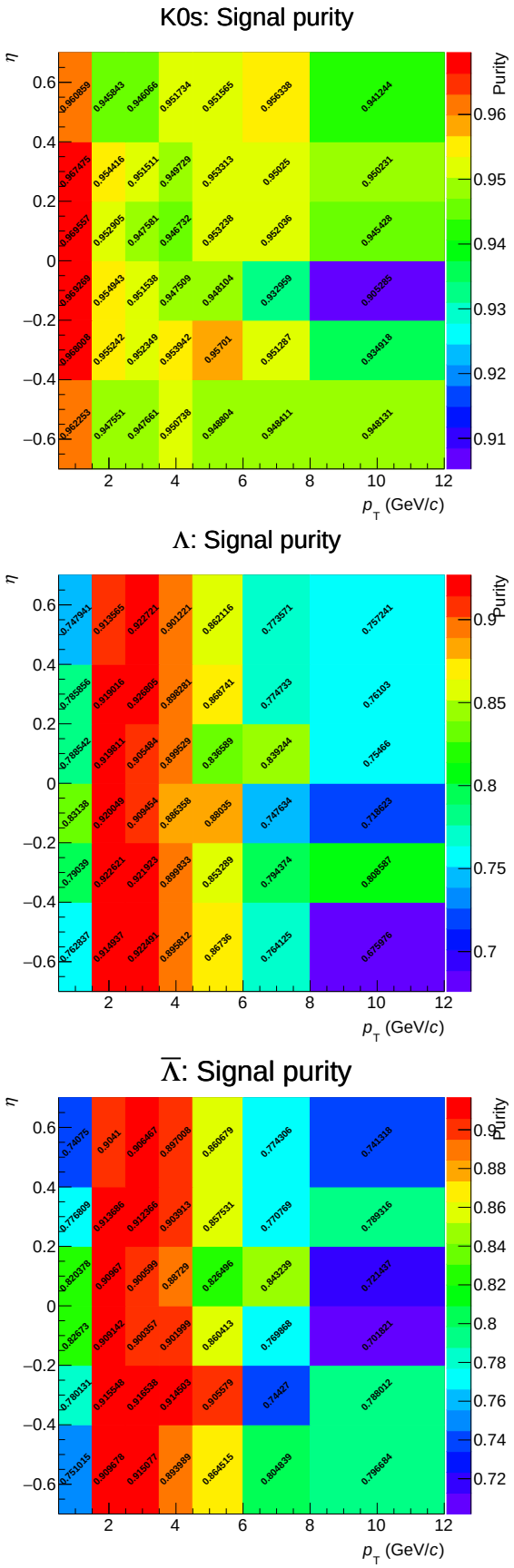

Figure 5.7: Purity of inclusive V^0 particles in various p_T and η bins used for estimation of uncorrected number of V^0 signal particles associated with jets: K^0_S (top), Λ (middle), $\overline{\Lambda}$ (bottom). Please note the different range of z axis.

5.7 Corrections

In order to obtain the physically interpretable results out of the raw yields of V^0 particles, several corrections need to be applied, namely the reconstruction efficiency and the $\Lambda/\overline{\Lambda}$ feed-down corrections of both inclusive and the associated V^0 production.

Apart from these corrections, an additional step would be a correction of the V^0 associated with jets for the particle produced in the so-called underlying event (UE). To describe UE, the following definition is possible: the underlying event comprises particles created by any possible production mechanism except for the processes with the high momentum transfer (i.e. the hard processes). In this particular case, there are several methods to estimate the UE production [42]. For example, the V^0 reconstruction in events with no reconstructed jets passing the selection criteria, in events where the jets are present but outside the jet cones, or in the artificial cones perpendicular to the reconstructed ones.

This correction plays an important role especially in the case of heavy-ion collisions, where the number of combinatorial jets and the background in general is quite high. In proton-proton collisions this contribution to the overall production is expected to be small due to the relatively small level of background contamination. For the purpose of this thesis, the UE correction is considered to be negligible, but will be further studied afterwards.

5.7.1 Reconstruction efficiency

Since the measured data are affected by the various detector effects, such as the finite detector resolution and granularity, momentum smearing, detector inefficient regions due to the construction and technical requirements as well as limited acceptance given by the detector geometry, obtained V^0 candidate yields need to be corrected for this finite detector response. This is done by applying the reconstruction efficiency, which is estimatedd based on the Monte Carlo (MC) based simulation. The resulting MC data are as close to the real collisions as possible and can be used as a suitable reference for real events.

The MC events are first generated by the `PYTHIA`, a program for simulating the high-energy physics events [45], then they undergo a full detector simulation via the `GEANT`, a set of tools used for a description of detector systems using MC based simulations of particle interaction with the matter [46]. Finally, the same reconstruction procedures and analysis cuts described in the previous sections are applied in order to mimic the real-data conditions.

In addition, the efficiency also includes the branching ratio of related decay channels of reconstructed V^0 candidates (meaning that no additional correction for this is needed once the efficiency is applied).

The reconstruction efficiency is defined as a ratio of associated ($N_{\mathrm{MC}}^{\mathrm{ass}}$) and generated ($N_{\mathrm{MC}}^{\mathrm{gen}}$) MC particles and generally can be a function of various kinematic quantities. In this analysis, the reconstruction efficiency of inclusive V^0 production is estimated independently for each V^0 particle and only the transverse momentum p_{T} dependence is considered[4] and given:

$$\epsilon^{\mathrm{incl}}(p_{\mathrm{T}}) = \frac{N_{\mathrm{MC}}^{\mathrm{ass}}(p_{\mathrm{T}})}{N_{\mathrm{MC}}^{\mathrm{gen}}(p_{\mathrm{T}})}. \tag{5.2}$$

For the proper estimation of the reconstruction efficiency MC generated particles have to fulfil following requirements:

[4] For the purpose of η–weighted method of efficiency estimation discussed later in this section, the η dependence is also considered.

- correct identity of both daughter tracks and mother particle (based on PDG code),
- mother particle has to be primary-like (close to the primary vertex),
- particle generated in the η region of interest.

If the generated particle passes the additional criteria listed below:

- V^0 candidate passes all selection criteria (as listed in Table 5.2),
- both daughter particles come from the same MC mother,
- invariant mass of V^0 candidate is within the signal region,

it is also considered to be the associated particle.

The resulting reconstruction efficiency of inclusive V^0 particles including the branching ratio of particular decay channels and the limited detector acceptance as a function of V^0 p_T is presented in Fig. 5.8. The reconstruction efficiencies of all three particle species exhibit a similar p_T dependency. With the increasing p_T, the reconstruction efficiency of inclusive V^0 particles increases, until it reaches maximum around $p_T \approx 4$ GeV/c, where its value is $\approx 40\%$ for K^0_S and $\approx 34\%$ in case of $\Lambda/\overline{\Lambda}$ particles. For a comparison, a single track reconstruction efficiency of primary charged particles is $\approx 60\%$ at $p_T = 0.15$ GeV/c and increases with the p_T. In the region of $1 < p_T < 10$ GeV/c it is uniform with a value of $\approx 87\%$ and slightly decreases for higher p_T [47].

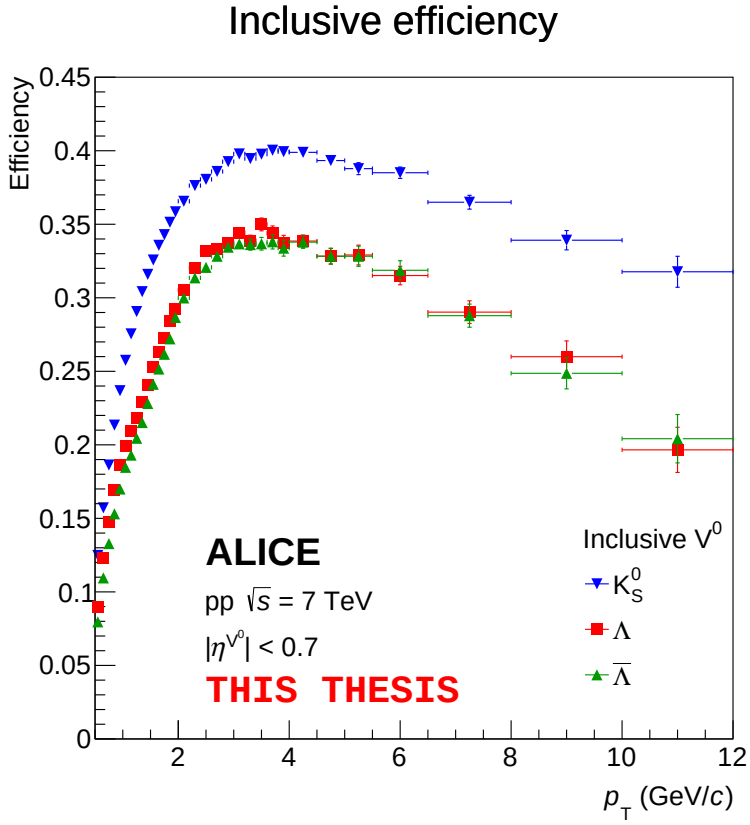

Figure 5.8: Reconstruction efficiency of inclusive K^0_S, Λ and $\overline{\Lambda}$ particles as a function of V^0 p_T.

The efficiency corrected p_{T} dependent yields ($N^{\mathrm{cor}}_{\mathrm{incl}}$) of inclusive $\mathrm{K}^0_{\mathrm{S}}$, Λ and $\overline{\Lambda}$ particles are then given

$$N^{\mathrm{cor}}_{\mathrm{incl}}(p_{\mathrm{T}}) = \frac{N^{\mathrm{raw}}_{\mathrm{incl}}(p_{\mathrm{T}})}{\epsilon^{\mathrm{incl}}(p_{\mathrm{T}})}, \tag{5.3}$$

where $N^{\mathrm{raw}}_{\mathrm{incl}}$ is an uncorrected (raw) yield obtained via the signal extraction described in previous section.

Pseudorapidity–weighted reconstruction efficiency

Since the shape of distribution of V^0 particles associated with the charged jets (in-jet V^0) differs from the inclusive one, the reconstruction efficiency exhibits a significant dependency not only on p_{T}, but on η as well. Therefore as already mentioned before, the V^0 candidates are divided not only based on their p_{T}, but into p_{T}–η bins in which the signal extraction procedure is then conducted individually. Moreover, the overall number of V^0 candidates associated with jets is much lower then the inclusive ones (and also divided into the higher number of bins), a modified η–weighted method for efficiency estimation is applied.

First, the corrected yield of in-jet V^0 particles in p_{T}–η bins is obtained based on

$$N^{\mathrm{cor}}_{\mathrm{injet}}(p_{\mathrm{T}}, \eta) = \frac{N^{\mathrm{raw}}_{\mathrm{injet}}(p_{\mathrm{T}}, \eta)}{\epsilon^{\mathrm{incl}}(p_{\mathrm{T}}, \eta)}, \tag{5.4}$$

where $N^{\mathrm{raw}}_{\mathrm{injet}}$ is the raw yield of *in-jet* V^0 particles obtained via the signal extraction and ϵ^{incl} is the MC driven reconstruction efficiency of *inclusive* V^0 particles (Eq. 5.2) obtained by the procedure described before. The difference here is that the efficiency depends both on p_{T} and η and thus has to be obtained in p_{T}–η bins, contrary to the purely inclusive case.

Then the η–weighted p_{T} dependent reconstruction efficiency for in-jet V^0 is obtained as a ratio of η–integrated $N^{\mathrm{injet}}_{\mathrm{real}}$ and $N^{\mathrm{cor}}_{\mathrm{injet}}$:

$$\epsilon^{\mathrm{injet}}(p_{\mathrm{T}}) = \frac{\sum_\eta N^{\mathrm{raw}}_{\mathrm{injet}}(p_{\mathrm{T}}, \eta)}{\sum_\eta N^{\mathrm{cor}}_{\mathrm{injet}}(p_{\mathrm{T}}, \eta)} = \frac{N^{\mathrm{raw}}_{\mathrm{injet}}(p_{\mathrm{T}})}{N^{\mathrm{cor}}_{\mathrm{injet}}(p_{\mathrm{T}})}. \tag{5.5}$$

The result of this data-driven approach is the reconstruction efficiency of in-jet $\mathrm{K}^0_{\mathrm{S}}$, Λ and $\overline{\Lambda}$ particles also including the branching ratio of relevant decay channels and the limited detector acceptance as a function of V^0 p_{T} which is shown in Fig. 5.9.

5.7.2 Feed-down subtraction

The final step for obtaining the fully corrected spectra is to evaluate the fraction of V^0 particles coming from decay of heavier particles, or commonly referred to as the feed-down fraction. The dominant decay channel considered in this analysis is the weak decay of multi-strange baryon $\Xi^{0,-} \longrightarrow \Lambda + \pi^{0,-}$ (and similarly for the charge conjugates) with the mean lifetime $\tau \approx 10^{-10}$ s [41]. For the brevity, only the case of Λ will be described.

The feed-down fraction f is defined simply as a ratio of measured yields of Λ coming from the Ξ decays ($N^{\Lambda\leftarrow\Xi}_{\mathrm{real}}$) and of all Λ particles ($N^{\Lambda}_{\mathrm{real}}$):

$$f^{\mathrm{incl}}(p^{\Lambda}_{\mathrm{T}}) = \frac{N^{\Lambda\leftarrow\Xi}_{\mathrm{real}}(p^{\Lambda}_{\mathrm{T}})}{N^{\Lambda}_{\mathrm{real}}(p^{\Lambda}_{\mathrm{T}})}. \tag{5.6}$$

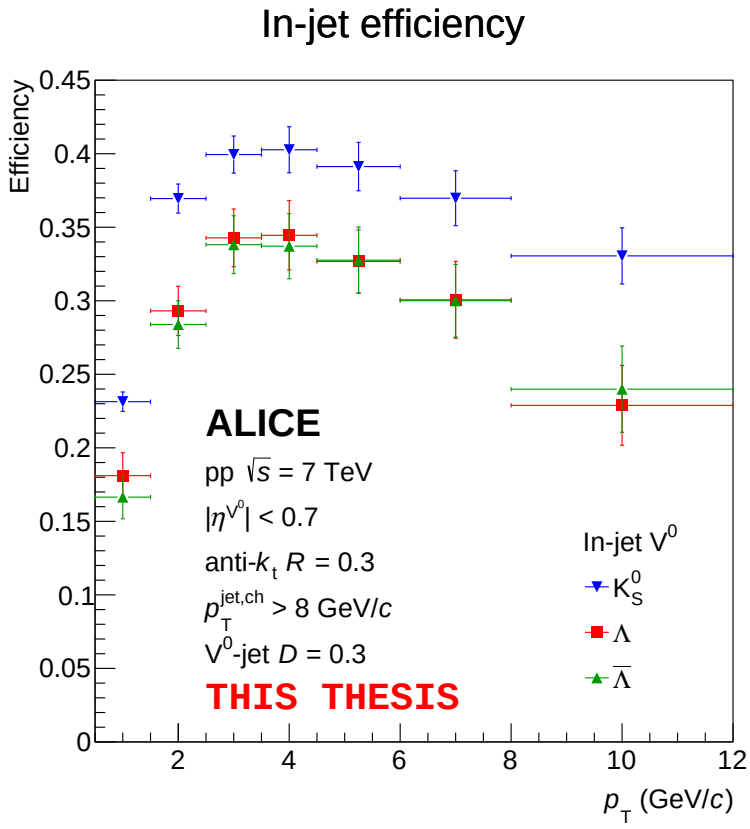

Figure 5.9: Reconstruction efficiency of K^0_S, Λ and $\overline{\Lambda}$ particles associated with the charged jets as a function of p_T obtained by the η–weighted method (Eq. 5.5). For details please see the text in this section.

Since we cannot distinguish between the prompt and the non-prompt (or secondary, i.e. from secondary decays) Λ particles directly in real data, the yield of secondary Λ particles is estimated using the MC driven approach is used. Similarly to the already discussed reconstruction efficiency estimation method, for each of the MC generated Λ particles its mother identity is first checked. If the Λ mother is identified as a Ξ, the Λ is then tagged as the secondary particle. The result of such procedure is a decay matrix $N^{\Lambda\leftarrow\Xi}_{\mathrm{MC}}(p^{\Lambda}_{\mathrm{T}}, p^{\Xi}_{\mathrm{T}})$ representing the distribution of all Λ particles (with momentum p^{Λ}_{T}) from the decays of Ξ (with momentum p^{Ξ}_{T}).

The yield of the real non-prompt Λ particles ($N^{\Lambda\leftarrow\Xi}_{\mathrm{real}}$) is given by:

$$N^{\Lambda\leftarrow\Xi}_{\mathrm{real}}(p^{\Lambda}_{\mathrm{T}}) = \sum_{p^{\Xi}_{\mathrm{T}}} N^{\Lambda\leftarrow\Xi}_{\mathrm{MC}}(p^{\Lambda}_{\mathrm{T}}, p^{\Xi}_{\mathrm{T}}) S(p^{\Xi}_{\mathrm{T}}) = \sum_{p^{\Xi}_{\mathrm{T}}} N^{\Lambda\leftarrow\Xi}_{\mathrm{MC}}(p^{\Lambda}_{\mathrm{T}}, p^{\Xi}_{\mathrm{T}}) \frac{N^{\Xi}_{\mathrm{real}}(p^{\Xi}_{\mathrm{T}})}{N^{\Xi}_{\mathrm{MC}}(p^{\Xi}_{\mathrm{T}})}, \tag{5.7}$$

where $S(p_T)$ is a scale factor. Its presence is due to the observed discrepancy between the MC generated and measured spectra of Ξ^- baryons. Even though `PYTHIA` describes the kinematics of such decays well, the absolute number of produced particles is not in agreement with the data. Thus the ratio of measured (published) and the MC generated spectra of Ξ^- baryons S is introduced in order to correct this discrepancy. The scale factor S is strongly p_T–dependent with the typical values in range $1 - 2.5$.

The feed-down fraction obtained by this procedure for the inclusive Λ and $\overline{\Lambda}$ particles is depicted in Fig. 5.10. Due to the limited statistics and therefore the relatively low number non-prompt Λ, the decay matrix $N^{\Lambda\leftarrow\Xi}_{\mathrm{MC}}$ is only sparsely populated, especially in

the region of higher p_{T}. This leads to the fact, that the estimated feed-down fraction decreases rapidly for $p_{\mathrm{T}} \geq 5$ GeV/c. Such observation would have meant, that in the high-p_{T} region all Λ or $\overline{\Lambda}$ particles are prompt which is very unlikely. To extend the estimation towards higher momentum, the feed-down fraction was fit with the linear function in the region of $1 \leq p_{\mathrm{T}} \leq 5$ GeV/c where the decay matrix population was sufficient. For the correction, the fitted function is used instead.

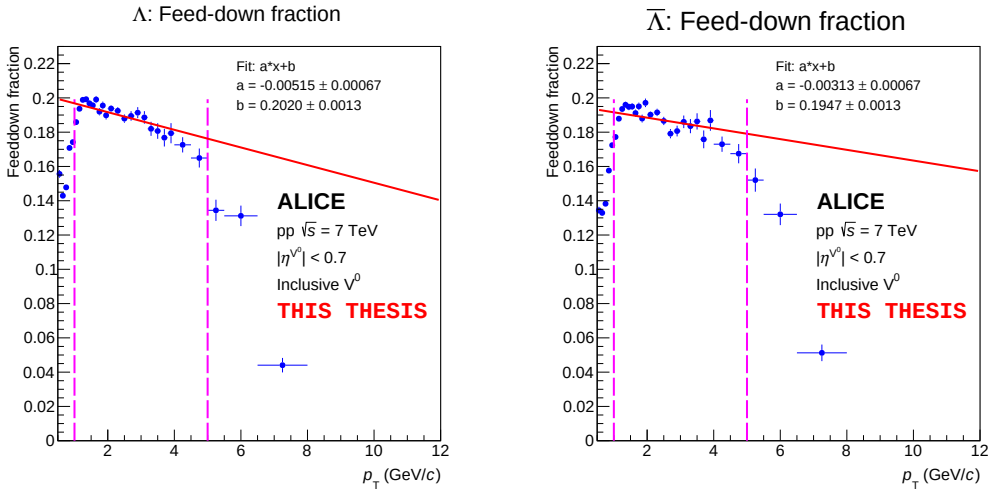

Figure 5.10: The feed-down fraction of inclusive Λ (left) and $\overline{\Lambda}$ (right) particles as a function of p_{T}. The solid line represents the linear function fitted in the region $p_{\mathrm{T}} = 1 - 5$ GeV/c indicated by the dashed vertical lines to expand the reach of the rapidly decreasing MC based estimation.

For correction of in-jet Λ and $\overline{\Lambda}$ yields, the estimation for inclusive V^0 feed-down fraction was obtained as described above. An assumption that $f^{\mathrm{injet}} = f^{\mathrm{incl}}$ based on MC study [42] is applied since any direct measurement of Ξ baryon associated with the jets has not been done yet.

5.8 Master formula for corrected spectra

The final relation between the initially extracted raw yields obtained via the signal extraction procedure and the final spectra fully corrected for the finite reconstruction efficiency, detector acceptance and the feed-down as a result of each correction steps described in the preceding sections is given by:

$$\mathcal{S}^{\mathrm{cor}}_{\mathrm{incl/injet}}(p_{\mathrm{T}}^{\mathrm{V}^0}) = \frac{1}{\mathcal{N}} \frac{N^{\mathrm{raw}}_{\mathrm{incl/injet}}(p_{\mathrm{T}}^{\mathrm{V}^0})}{\epsilon^{\mathrm{incl/injet}}(p_{\mathrm{T}}^{\mathrm{V}^0})} \Big(1 - f^{\mathrm{incl}}(p_{\mathrm{T}}^{\Lambda/\bar{\Lambda}})\Big), \tag{5.8}$$

where $\mathcal{S}^{\mathrm{cor}}$ is the fully corrected normalised spectrum of V^0 particles, N^{raw} is the raw yield of V^0 particles obtained via the signal extraction procedure, ϵ is the relevant reconstruction efficiency, f is the feed-down fraction (only applicable for Λ and $\overline{\Lambda}$ particles, in case of $\mathrm{K}^0_{\mathrm{S}}$ this term is not present) given by Eq. (5.6) and the $\mathcal{N}$ is normalisation.

The normalisation in this particular analysis is chosen in the following way. The yields are divided by the total number of events passing all selection criteria and quality requirements listed in Sec. 5.2, the $|\eta^{\mathrm{V}^0}|$ acceptance and width of the given p_{T} bin.

Chapter 6

Results

6.1 Inclusive production of identified V^0 particles

In this section, the fully corrected spectra and baryon-meson ratio of inclusive V^0 particles produced in pp collisions at $\sqrt{s} = 7$ TeV are presented. The results of this analysis are compared with the preliminary results of independent analysis carried out within the ALICE Physics Working Group Light Flavour (PWG-LF) [43] shown in Fig. 3.2. For the proper comparison, the following changes with respect to the selection criteria listed in Tab. 5.2 was introduced to match the original analysis.

First, the V^0 pseudorapidity acceptance $|\eta^{V0}| \leq 0.7$ was replaced by the V^0 rapidity acceptance $|y^{V0}| \leq 0.5$. Second, an additional constraint for the particle identification have been applied, explicitly the TPC dE/dx maximal limit of 5σ for all of the V^0 daughter particles, i.e. π^+, π^-, p and $\bar{p}$ (as shown in Tab. 5.1). For the V^0 topological reconstruction exactly the same analysis class and the following signal extraction procedure has been used as described in the previous sections.

The event selection and the V^0 reconstruction procedure was conducted on the data from the same run list as in case of the original analysis [43], which is a different subset of LHC10d period than the one mentioned in the Sec. 5.1. Specifically, the following list of runs has been used: 126097, 125855, 125851, 125850, 125849, 125848, 125847, 125101, 125100,125097, 125085, 126090, 126008, 126007, 126004, 125844, 125843, 125842, 125633, 125632, 125630, 125186,126158, 126088, 126082, 126081, 126078, 122374, 126409, 126408, 126407, 126359, 126352, 126437, 126432,126425, 126424, 126422, 126406, 126405, 126404, 126403, 126351, 126285, 126284, 126283, 126168, 126167, 126160.

Also, newer MC data sample LHC14j4d reproduced in 2014 but anchored to the same old LHC10d dataset have been used for the estimation of reconstruction efficiency and the feed-down fraction instead of the originally used LHC10f6a dataset.

It should be pointed out here, that the original analysis was done with the data in the old ESD format, which was later superseded with the new AOD format. During this transition the data was in fact reproduced and thus the difference between the original and the current data sample may be present (for instance in a form of different overall number of events, track resolution and reconstruction efficiency, etc.).

6.1.1 Normalisation discussion

Since not only the final ratio has been compared, but the spectra of the inclusive K^0_S and Λ particles corrected for both the reconstruction efficiency and the feeddown as well, in order to verify the analysis procedure, also the same normalisation has to be applied. Otherwise the normalisation would not play a role in the comparison, because it cancels out in the final Λ/K^0_S ratio.

For the purpose of this particular analysis the spectra of produced V^0 particles are normalised by the number of events passing the selection criteria listed in Sec. 5.2 and the unit area in $p_T \times \eta$ space. However, the spectra used for the ratio in the original analysis

are normalised to the number of inelastic collisions, which are not directly accessible from the data sample. Therefore the modified normalisation estimation based on the method provided by the author of the PWG-LF study [48] described bellow is used.

Since no detector is able to record and store every inelastic (Inel) collision due to the limited data taking frequency, every analysis is in general performed only on a subset of these collisions, the so-called triggered collisions (Trig), such as the MB used in this analysis. Moreover, the analyses usually require fulfilling additional conditions in a form of event selection based on the primary vertex reconstruction quality (Vtx) and its maximal longitudinal distance (PVZ) from the detector centre. Appropriate number of events (N) and the number signal particles (S) corresponds to each of these event classes and the general relations hold:

$$N_{\mathrm{Inel}} \geq N_{\mathrm{Trig}} \geq N_{\mathrm{Vtx}} \geq N_{\mathrm{PVZ}}, \tag{6.1}$$

$$S_{\mathrm{Inel}} \geq S_{\mathrm{Trig}} \geq S_{\mathrm{Vtx}} \geq S_{\mathrm{PVZ}}. \tag{6.2}$$

But it is important to realise that $N_{\mathrm{A}}/N_{\mathrm{B}} \neq S_{\mathrm{A}}/S_{\mathrm{B}}$ for the two different event classes A and B.

Therefore the following relation has to be applied to obtain consistently normalised yields

$$\frac{S_{\mathrm{Inel}}}{N_{\mathrm{Inel}}} = \frac{C}{N_{\mathrm{Trig}}} \cdot \frac{N_{\mathrm{Vtx}}}{N_{\mathrm{PVZ}}} \cdot \frac{S_{\mathrm{meas}}}{\epsilon_{\mathrm{meas}}}, \tag{6.3}$$

where S_{meas} and ϵ_{meas} is the number of signal particles extracted after all selection criteria are imposed and the corresponding reconstruction efficiency respectively. The trigger efficiency $C = N_{\mathrm{Trig}}/N_{\mathrm{Inel}} \approx 0.852$ is provided by the independent analysis [43] in order to estimate the overall number of inelastic collisions. Therefore the left-hand side of Eq. (6.3) represents the normalised spectrum used in the original study and the last term of right-hand side is the corrected yield of V^0 particles obtained by the procedure described in this chapter.

6.1.2 Grand comparison

The comparison between the PWG-LF Spectra group analysis [43] and this analysis is presented for each analysis step. The general notation is the following: the data from the original analysis are marked by open blue circles and the results of this analysis by full red circles. The bottom panel of each comparison plots indicates the ratio, where the nominator contains the result from this analysis and the denominator the original one.

First, the final reconstruction efficiency as a function of V^0 p_{T} including also the detector acceptance obtained according to the procedure described in Sec. 5.7.1 for the inclusive $\mathrm{K}^0_{\mathrm{S}}$ and Λ particles is shown in Fig. 6.1. Please note, that a slightly different method for efficiency estimation was used in the original study which may be reflected in the difference between the two analyses. Contrary to the efficiency obtained after imposing the event selection criteria on Monte Carlo events as used in this analysis, the efficiency in the original one was estimated using all the particles from all MC events, i.e. before applying any event selection criteria on the MC data sample.

In Fig. 6.2 the fraction of Λ particles coming from decays of multi-strange Ξ baryons is shown. The blue line indicates the result of linear function fit used for estimation of the feed-down fraction due to limited statistics especially in the high-p_{T} region as described in Sec. 5.7.2.

The spectra of inclusively produced $\mathrm{K}^0_{\mathrm{S}}$ and Λ particles corrected both for the reconstruction efficiency and the feed-down normalised to the number of inelastic events

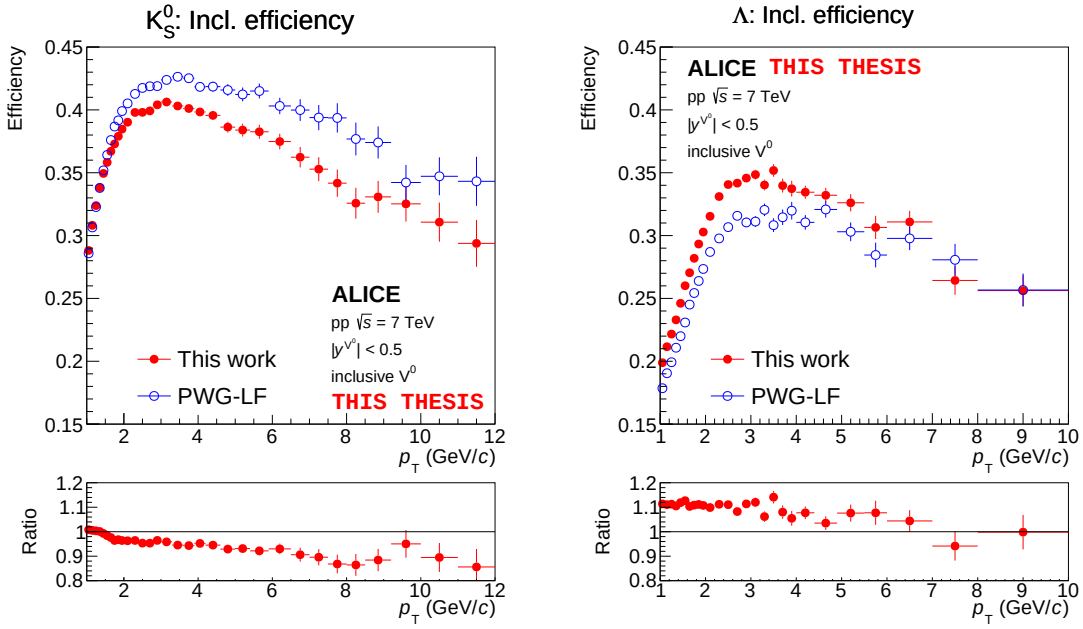

Figure 6.1: The comparison of reconstruction efficiency of inclusive V^0 particles from this analysis (blue) with the original one (red) altogether with their ratio (bottom panel): K^0_S (left) and Λ (right).

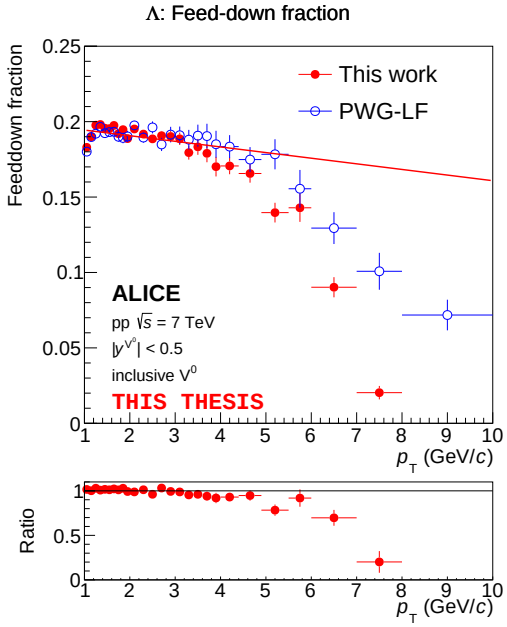

Figure 6.2: The comparison of the feed-down fraction of inclusive Λ particles estimated in this analysis (blue) and the original one (red) altogether with their ratio (bottom panel). The blue line indicates the linear fit used for feeddown estimation (see Sec. 5.7.2).

and the unit area in $p_T \times \eta$ space are shown in Fig. 6.3. From this spectra the final p_T-dependent baryon-meson ratio of inclusive V^0 particles have been extracted and is presented in Fig. 6.4.

As can be seen, both the spectra and the ratio produced by the procedure described

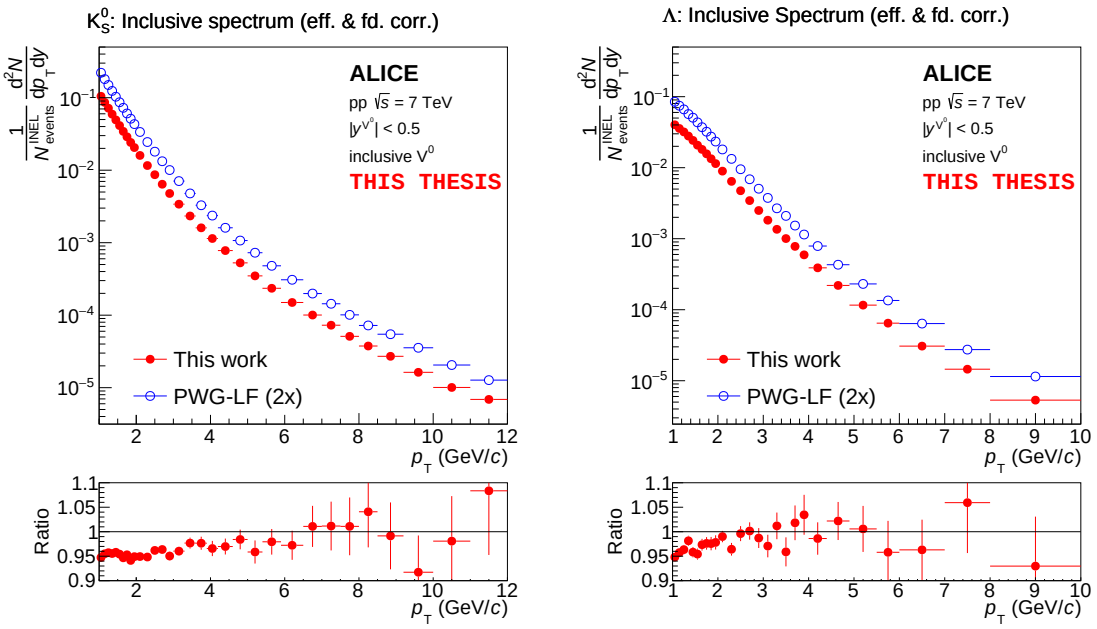

Figure 6.3: The comparison of corrected inclusive V^0 spectra from this analysis (blue) with the original one (red) altogether with their ratio (bottom panel): K^0_S (left) and Λ (right).

in this chapter are compatible within 5% (and with respect to the statistical uncertainty) with the results of the original study in the wide p_T range from 1 GeV/c to 10 GeV/c. This confirms that the methodology used in this thesis can be considered to be fully verified.

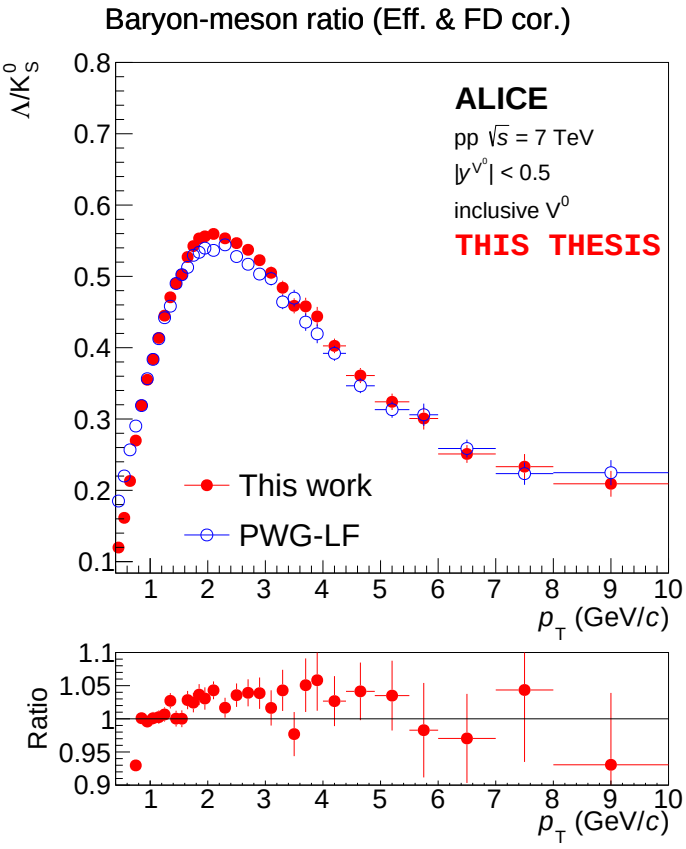

Figure 6.4: The comparison of the inclusive $\Lambda/\mathrm{K}^0_\mathrm{S}$ ratio estimated in this analysis (blue) and the original one (red) as can be seen in Fig. 3.2 altogether with their ratio (bottom panel).

6.2 Identified V^0 particles associated with charged jets

In this section, the principal up-to-date results of the still ongoing analysis of neutral strange particle production of K^0_S, Λ and $\overline{\Lambda}$ particles associated with the charged jets in proton-proton collision at $\sqrt{s} = 7$ TeV are presented. Namely, the corrected p_T-dependent spectra and the baryon-meson ratio.

6.2.1 Transverse momentum spectra

Both inclusive spectra of K^0_S, Λ and $\overline{\Lambda}$ particles and the ones associated with charged jets as a function of V^0 p_T in range $1 - 10$ GeV/c produced in pp collisions at $\sqrt{s} = 7$ TeV corrected for the reconstruction efficiency and the feed-down normalised to the number of events passing selection criteria listed in Sec. 5.2 and unit area in $p_\mathrm{T} \times \eta$ space are presented in Fig. 6.5.

As can be seen, even though the general trend of the spectra of V^0s associated with charged jets is similar to the inclusive production, the overall shape differs. In the case of the all three V^0 species associated with charged jets a spectra hardening (spectra falls less steeply with increasing p_T) is observed with respect to the inclusively produced particles.

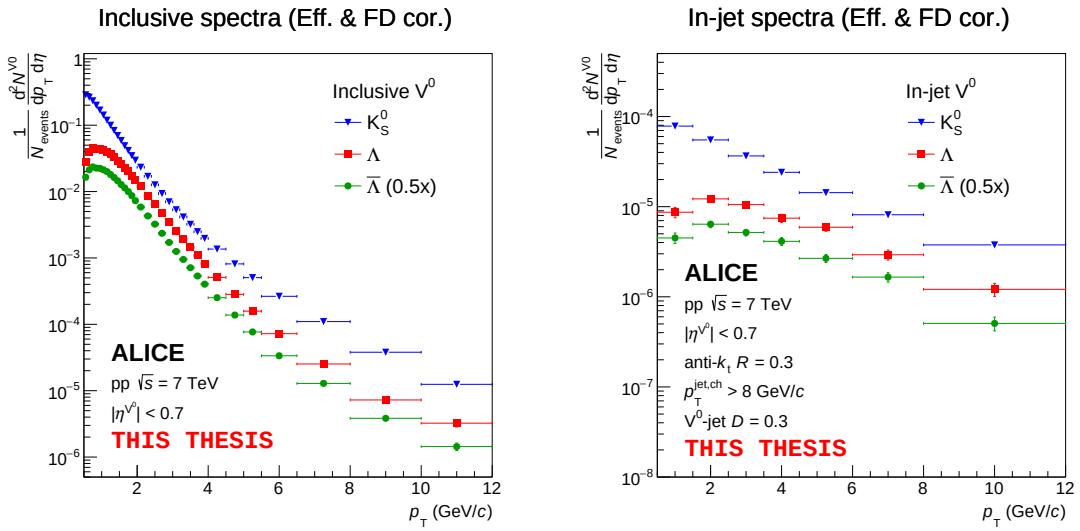

Figure 6.5: The reconstructed efficiency and feed-down corrected p_{T}-differential spectra of inclusive V^0 particles (left) and V^0 particle production associated with the charged jets (right) normalized by the number of events passing selection criteria and the unit area in $p_{\mathrm{T}} \times \eta$ space.

6.2.2 Baryon-meson ratio of neutral strange particles

The baryon-meson ratio of neutral strange $\mathrm{K}^0_{\mathrm{S}}$, Λ and $\overline{\Lambda}$ particles associated with the charged jets reconstructed with the anti-k_{T} algorithm extracted from the reconstruction efficiency and feed-down corrected p_{T}-dependent spectra is presented in this section. Additionally, the results of a study of its dependency on various parameters, namely the jet resolution parameter R, V^0-jet matching distance D and minimum jet p_{T}, are shown. Please note, that contrary to the case of the inclusive $\Lambda/\mathrm{K}^0_{\mathrm{S}}$ ratio discussed in Sec. 6.2, the results of the baryon-meson ratio $(\Lambda + \bar{\Lambda})/(2\mathrm{K}^0_{\mathrm{S}})$ presented in this section also include the $\overline{\Lambda}$ particles in a form of the average of Λ and $\overline{\Lambda}$ production.

The baryon-meson ratio of V^0 associated with the charged jets reconstructed with three values of jet resolution parameter $R = \{0.2, 0.3, 0.4\}$ and the related V^0-jet matching parameter $D = R$ compared to the ratio of inclusively produced V^0 as a function of V^0 p_{T} in range of $1 - 10$ GeV/c is presented in Fig. 6.6. When compared to the inclusive case, the ratio exhibits a similar magnitude with respect to the statistical uncertainties. However, the peak position is shifted towards higher p_{T} which results in the situation that in the region of $p_{\mathrm{T}} > 4.5$ GeV/c the ratio is above the inclusive one and therefore a slight enhancement of $\mathrm{K}^0_{\mathrm{S}}$ production associated with the charged jets is observed.

Considering the outcome of the jet sample reconstructed with the various jet resolution parameters R, Fig. 6.6 indicates that ratio of V^0s associated with charged jets does not depend significantly on the value within the statistical uncertainty. Since the value of V^0-jet matching parameter D (or the distance between V^0 and the jet axis in $\eta \times \phi$ space) is directly related to jet resolution parameter R, this therefore indicates that the production associated with the jets is not much sensitive to the finite size of the jet cones in proton-proton collisions. This however might be no longer valid in case of heavy-ions collisions, where the jets are generally more influenced by the higher background contamination.

In order to investigate the influence of jet reconstruction parameters further, the results of baryon-meson ratio of V^0 particles associated with charged jets reconstructed with the same R and various values of V^0-jet matching parameters D are shown in Fig. 6.7. Similarly

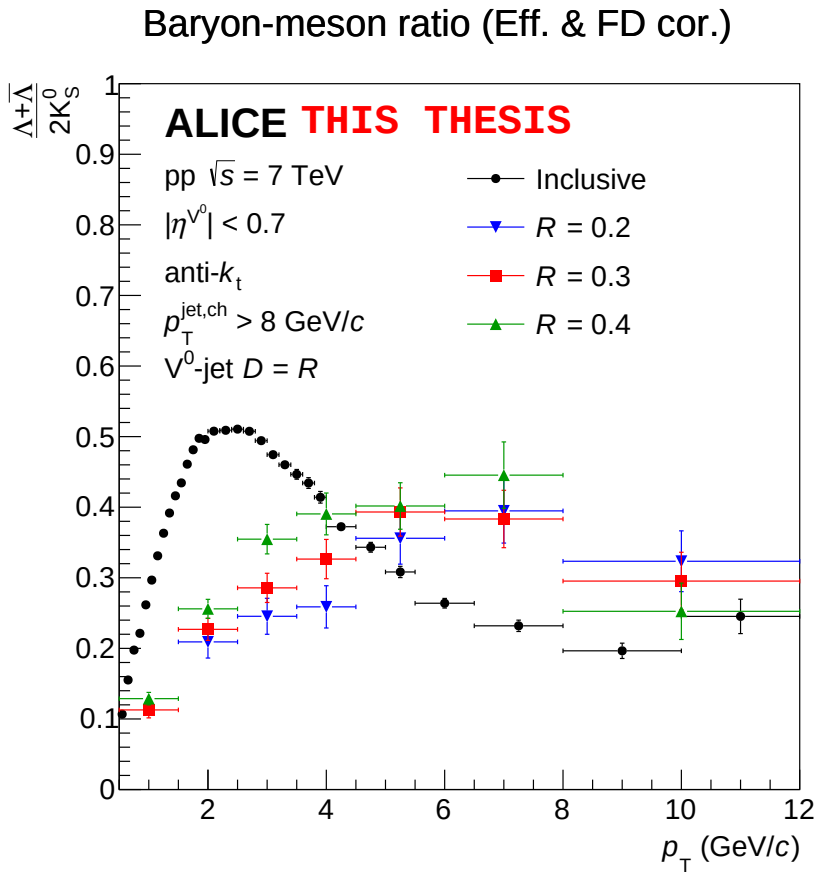

Figure 6.6: The reconstruction efficiency and feed-down corrected baryon-meson ratio of V^0 particles associated with the charged jets with $p_T^{jet,ch} > 8$ GeV/c and the same V^0-jet matching distance $D = R$ in pp collision at $\sqrt{s} = 7$ TeV for three values of jet resolution parameter R (colour) compared to the ratio of inclusive V^0 production (black) as a function of V^0 p_T.

to the jet resolution parameter, within the statistical uncertainties the result is independent of the V^0-jet matching distance value in the whole region of p_T.

Last, but not least, the baryon-meson ratio dependence on the minimum jet $p_T^{jet,ch}$ selection criterion is depicted in Fig. 6.8. In this figure, the baryon-meson ratio for three different values of the minimum $p_T^{jet,ch}$ can be seen. Contrary to the previously discussed results, in this case a systematic trend can be observed. As the minimum $p_T^{jet,ch}$ increases the value of baryon-meson ratio decreases in the intermediate p_T region, which means the number of $\Lambda/\overline{\Lambda}$ with respect to K_S^0 inside the charged jets decreases. This is manifested most clearly in the case of the softest jet selection criterion applied, $p_T^{jet,ch} > 5$ GeV/c. However, such threshold for jet p_T might be too low even in the case of pp collisions, and the resulting jet sample may still contain a relatively significant fraction of combinatorial jets biasing the final result since no additional constrain of jet selection is applied.

In order to arrive to final physically interpretable results, following studies are still needed: besides the already mentioned underlying event correction (Sec. 5.7), a systematic study of contribution of not-constrained tracks present in hybrid tracks sample will be performed together with a detailed study of systematic uncertainties originating from topological selection criteria, signal extraction procedure, feed-down contribution, etc. These studies are however beyond the scope of the Master's thesis.

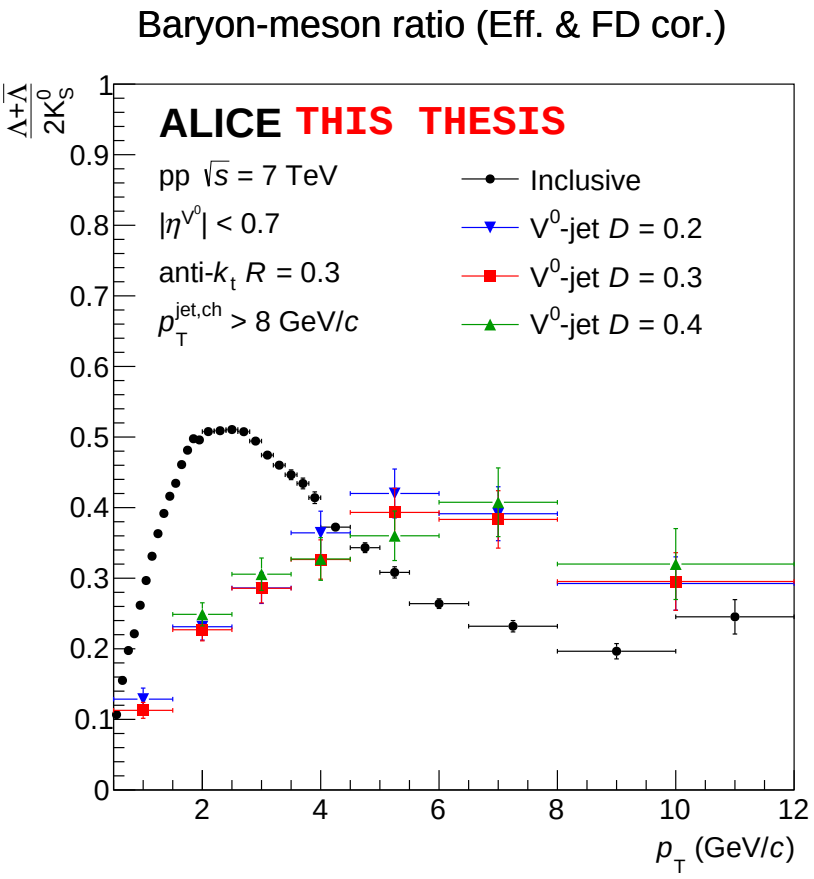

Figure 6.7: The dependency of reconstruction efficiency and feed-down corrected baryon-meson ratio of V^0 particles associated with the charged jets on the V^0-jet matching distance D for the jets with the resolution $R = 0.3$ and minimum $p_{\mathrm{T}}^{\mathrm{jet,ch}} > 8$ GeV/c (colour) compared to the ratio of inclusive V^0 production (black) as a function of V^0 p_{T}.

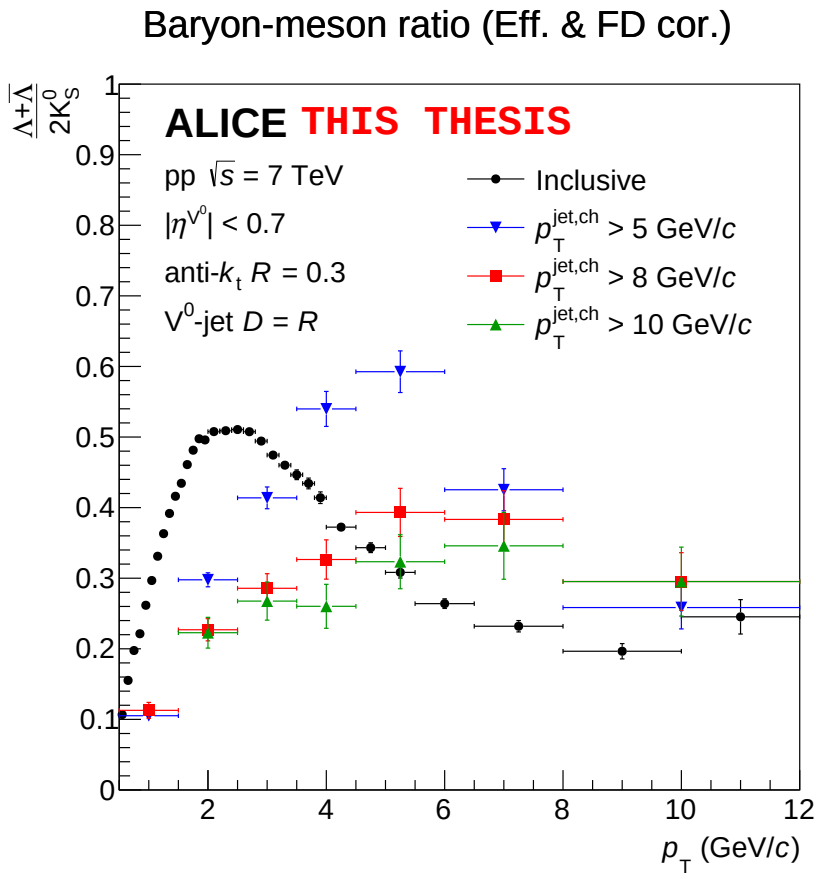

Figure 6.8: The dependency of reconstruction efficiency and feed-down corrected baryon-meson ratio of V^0 particles associated with the charged jets on the minimum $p_T^{jet,ch}$ for the jets with the resolution $R = 0.3$ and the same V^0-jet matching distance $D = 0.3$ (colour) compared to the ratio of inclusive V^0 production (black) as a function of V^0 p_T.

Summary

The aim of this thesis was to study the neutral strange particle production in proton-proton collisions at the LHC. In particular, the inclusive production of K^0_S, Λ and $\overline{\Lambda}$ together with novel measurements of strange particle production associated with jets was investigated.

Hadron identification in jets carries crucial information about the parton fragmentation process and the following hadronisation. This process is still not fully understood, especially concerning the neutral strange hadron production and is therefore currently under study in the experiments both at the LHC and RHIC. The results of proton-proton collisions provide not only the insights of the discussed topic but will also be used as baseline for the currently ongoing studies of p-Pb and Pb-Pb collisions.

The topological reconstruction and selection of V^0 particles in the p_T range of $1 - 12$ GeV/c was conducted on a minimum-bias sample of pp collisions at $\sqrt{s} = 7$ TeV measured with the ALICE detector. The fully corrected transverse momentum spectra of K^0_S, Λ and $\overline{\Lambda}$ and their respective baryon-meson ratio were measured. The results are in a very good agreement (within the 5%) with an independent analysis carried out in another Physics Working Group of the ALICE Collaboration. This was a necessary step to verify the used methodology described in Chapter 5.

In the next step, a detailed analysis of identified K^0_S, Λ and $\overline{\Lambda}$ production associated with charged jets reconstructed with the anti-k_T jet finding algorithm was performed. The resulting p_T spectra corrected for the reconstruction efficiency, detector acceptance and the $\Lambda/\overline{\Lambda}$ feed-down from heavier multi-strange Ξ baryons were presented in Section 6.2.1 for both inclusive particles and V^0 associated with charged jets.

The neutral strange baryon-meson ratio of Λ, $\overline{\Lambda}$ and K^0_S particles associated with the charged jets was presented in Section 6.2.2 together with the results of a differential study of its dependence on various jet reconstruction related parameters. No significant dependence on jet resolution parameter or V^0–jet matching distance was observed, however its behaviour changes significantly with the value of minimum jet p_T selection criterion.

These preliminary results of strange particle production associated with charged jets will be further complemented by a detailed study of systematic uncertainties and the contribution of not-constrained tracks present in hybrid tracks sample as well as correction of the V^0 spectra for the underlying event contribution. This goes beyond the scope of the Master's thesis.

Bibliography

[1] V. Kučera, *Production of strange particles in charged jets in Pb-Pb and p-Pb collisions measured with ALICE*, *J.Phys.: Conf. Ser.* **612** (2015) 012013.

[2] **STAR** Collaboration, B. Abelev *et. al.*, *Energy dependence of $\pi^{\pm}$, p and anti-p transverse momentum spectra for Au+Au collisions at $\sqrt{s_{\rm NN}}$ = 62.4 and 200-GeV*, *Phys.Lett.* **B655** (2007) 104–113 [nucl-ex/0703040].

[3] **STAR** Collaboration, M. Lamont, *Identified particles at large transverse momenta in STAR in Au+Au collisions at $\sqrt{s_{\rm NN}}$ = 200-GeV*, *J.Phys.* **G30** (2004) S963–S968 [nucl-ex/0403059].

[4] **ALICE** Collaboration, B. B. Abelev *et. al.*, *K^0_S and Λ production in Pb-Pb collisions at $\sqrt{s_{\rm NN}}$ = 2.76 TeV*, *Phys.Rev.Lett.* **111** (2013) 222301 [1307.5530].

[5] M. Gyulassy, I. Vitev, X.-N. Wang and B.-W. Zhang, *Jet quenching and radiative energy loss in dense nuclear matter*, nucl-th/0302077.

[6] R. J. Fries, B. Muller, C. Nonaka and S. A. Bass, *Hadronization in heavy ion collisions: Recombination and fragmentation of partons*, *Phys. Rev. Lett.* **90** (2003) 202303 [nucl-th/0301087].

[7] R. J. Fries, V. Greco and P. Sorensen, *Coalescence Models For Hadron Formation From Quark Gluon Plasma*, *Ann. Rev. Nucl. Part. Sci.* **58** (2008) 177–205 [0807.4939].

[8] R. Serway, C. Moses and C. Moyer, *Modern Physics*. Cengage Learning, 2004.

[9] "The Nobel Prize in Physics 2004." http://www.nobelprize.org/nobel_prizes/physics/laureates/2004/. Online. 16.3.2016.

[10] K. Yagi, T. Hatsuda and Y. Miake, *Quark-Gluon Plasma: From Big Bang to Little Bang*. Cambridge monographs on particle physics, nuclear physics, and cosmology. Cambridge Univ. Press, Cambridge, 2005.

[11] C. Nattrass, "The quark gluon plasma." http://www.quantumdiaries.org/2010/04/26/the-quark-gluon-plasma/. Accessed: 2016-04-10.

[12] Y. Aoki, G. Endrodi, Z. Fodor, S. D. Katz and K. K. Szabo, *The Order of the quantum chromodynamics transition predicted by the standard model of particle physics*, *Nature* **443** (2006) 675–678 [hep-lat/0611014].

[13] R. Hagedorn, *Statistical thermodynamics of strong interactions at high energies. 3. Heavy-pair (quark) production rates*, *Nuovo Cim. Suppl.* **6** (1968) 311–354.

[14] P. Braun-Munzinger, V. Koch, T. Schäfer and J. Stachel, *Properties of hot and dense matter from relativistic heavy ion collisions*, *Phys. Rept.* **621** (2016) 76–126 [1510.00442].

[15] R. Stock, *Relativistic Nucleus-Nucleus Collisions and the QCD Matter Phase Diagram*, 0807.1610.

[16] J. Rafelski, *Strangeness production in the quark gluon plasma*, *Nuclear Physics A* **418** (1984) 215 – 235.

[17] J. Schukraft, *Heavy ion physics at the Large Hadron Collider: what is new? What is next?*, *Phys. Scripta* **T158** (2013) 014003 [1311.1429].

[18] S. Schuchmann and H. Appelshaeuser, *Modification of K_s^0 and $\Lambda(\overline{\Lambda})$ transverse momentum spectra in Pb-Pb collisions at $\sqrt{sNN}$ = 2.76 TeV with ALICE*. PhD thesis, Frankfurt U., Apr, 2015. Presented 22 Jul 2015.

[19] **ALICE** Collaboration, B. B. Abelev *et. al.*, *Multi-strange baryon production at mid-rapidity in Pb-Pb collisions at $\sqrt{s_{NN}}$ = 2.76 TeV*, *Phys. Lett.* **B728** (2014) 216–227 [1307.5543]. [Erratum: Phys. Lett.B734,409(2014)].

[20] Y. L. Dokshitzer and D. E. Kharzeev, *Heavy quark colorimetry of QCD matter*, *Phys. Lett.* **B519** (2001) 199–206 [hep-ph/0106202].

[21] D. d'Enterria, *Jet quenching*, 0902.2011.

[22] A. Andronic *et. al.*, *Heavy-flavour and quarkonium production in the LHC era: from proton–proton to heavy-ion collisions*, *Eur. Phys. J.* **C76** (2016), no. 3 107 [1506.03981].

[23] **ALICE** Collaboration, B. Abelev *et. al.*, *Measurement of charged jet suppression in Pb-Pb collisions at $\sqrt{s_{NN}}$ = 2.76 TeV*, *JHEP* **03** (2014) 013 [1311.0633].

[24] G. C. Blazey, J. R. Dittmann, S. D. Ellis, V. D. Elvira, K. Frame *et. al.*, *Run II jet physics*, hep-ex/0005012.

[25] G. P. Salam and G. Soyez, *A Practical Seedless Infrared-Safe Cone jet algorithm*, *JHEP* **05** (2007) 086 [0704.0292].

[26] M. Cacciari, G. P. Salam and G. Soyez, *The Anti-k_{T} jet clustering algorithm*, *JHEP* **0804** (2008) 063 [0802.1189].

[27] J. Tseng and H. Evans, *Sequential recombination algorithm for jet clustering and background subtraction*, *Phys. Rev.* **D88** (2013) 014044 [1304.1025].

[28] M. Cacciari, G. P. Salam and G. Soyez, *FastJet User Manual*, *Eur.Phys.J.* **C72** (2012) 1896 [1111.6097].

[29] M. Cacciari and G. P. Salam, *Dispelling the N^3 myth for the k_{T} jet-finder*, *Phys.Lett.* **B641** (2006) 57–61 [hep-ph/0512210].

[30] Y. L. Dokshitzer, G. D. Leder, S. Moretti and B. R. Webber, *Better jet clustering algorithms*, *JHEP* **08** (1997) 001 [hep-ph/9707323].

[31] **PHENIX** Collaboration, S. S. Adler *et. al.*, *Scaling properties of proton and anti-proton production in $\sqrt{s_{\mathrm{NN}}}$ 200-GeV Au+Au collisions*, *Phys. Rev. Lett.* **91** (2003) 172301 [nucl-ex/0305036].

[32] D. Molnar and S. A. Voloshin, *Elliptic flow at large transverse momenta from quark coalescence*, *Phys. Rev. Lett.* **91** (2003) 092301 [nucl-th/0302014].

[33] X. Sanchez Castro and C. Kuhn, $\mathrm{K}^0_{\mathrm{S}}$ *and* Λ *production associated to high-p_{T} particles in Pb-Pb collisions at $\sqrt{s_{\mathrm{NN}}}$ = 2.76 TeV with ALICE: Comparison between soft- and hard-processes in hadron production.* PhD thesis, Strasbourg U., Jun, 2015. Presented 31 Mar 2015.

[34] **STAR** Collaboration, C. Adler *et. al.*, *Disappearance of back-to-back high p_T hadron correlations in central Au+Au collisions at $\sqrt{s_{NN}}$ = 200-GeV*, *Phys. Rev. Lett.* **90** (2003) 082302 [nucl-ex/0210033].

[35] **ALICE** Collaboration, V. Kučera, *Production of strange particles in charged jets in Pb–Pb and p–Pb collisions measured with ALICE*, in *7th International Conference on Hard and Electromagnetic Probes of High-Energy Nuclear Collisions (Hard Probes 2015) Montréal, Québec, Canada, June 29-July 3, 2015*, 2015. 1511.02766.

[36] **ALICE** Collaboration, A. Zimmermann, *Production of strange particles in charged jets in p–Pb and Pb–Pb collisions measured with ALICE at the LHC*, in *10th International Workshop on High-pT Physics in the RHIC/LHC Era (HPT 2014) Nantes, France, September 9-12, 2014*, 2015. 1502.01263.

[37] **ALICE** Collaboration, X. Zhang, K^0_S *and* Λ *production in charged particle jets in p–Pb collisions at* $\sqrt{s_\mathrm{NN}} = 5.02$ *TeV with ALICE*, *Nucl. Phys.* **A931** (2014) 444–448 [1408.2672].

[38] **ALICE** Collaboration, K. Aamodt *et. al.*, *The ALICE experiment at the CERN LHC*, *JINST* **3** (2008) S08002.

[39] J. Allen, C. Bernard, O. Bourrion, M. Chala, M. Del Franio, O. Driga, F. Fichera, N. Giudice, A. Grimaldi, P. Laloux, Q. Li, F. Librizzi, G. Liu, C. Loizides, G. Marcotte, S. Muggeo, J. F. Muraz, F. Noto, A. Orlandi, V. Petrov, F. Pompei, W. Qian, J. Rasson, S. Sakai, M. Salemi, M. Sharma, V. Sparti, J. S. Stutzmann, A. Timmons, A. Viticchie, M. Wang, X. Xiang, F. Zhang, J. Zhou and X. Zhu, *ALICE DCal: An Addendum to the EMCal Technical Design Report Di-Jet and Hadron-Jet correlation measurements in ALICE*, Tech. Rep. CERN-LHCC-2010-011. ALICE-TDR-14-add-1, CERN, Geneva, Jun, 2010.

[40] R. Brun and F. Rademakers, *ROOT: An object oriented data analysis framework*, *Nucl. Instrum. Meth.* **A389** (1997) 81–86.

[41] **Particle Data Group** Collaboration, K. A. Olive *et. al.*, *Review of Particle Physics*, *Chin. Phys.* **C38** (2014) 090001.

[42] V. Kučera and A. Zimmermann, *Production of K^0_S, Λ and $\overline{\Lambda}$ particles in charged jets in Pb-Pb collisions at $\sqrt{s_\mathrm{NN}}$ = 2.76 TeV measured with ALICE*, *ALICE Analysis Note*.

[43] Chinellato, D. David , *K^0_S, Λ and $\overline{\Lambda}$ production in proton-proton collisions at $\sqrt{s}$ = 7 TeV*, *ALICE Analysis Note*.

[44] M. Cacciari, G. P. Salam and G. Soyez, *FastJet User Manual*, *Eur. Phys. J.* **C72** (2012) 1896 [1111.6097].

[45] T. Sjostrand, S. Mrenna and P. Z. Skands, *PYTHIA 6.4 Physics and Manual*, *JHEP* **05** (2006) 026 [hep-ph/0603175].

[46] R. Brun, F. Bruyant, F. Carminati, S. Giani, M. Maire, A. McPherson, G. Patrick and L. Urban, *GEANT Detector Description and Simulation Tool*, .

[47] **ALICE** Collaboration, B. B. Abelev *et. al.*, *Charged jet cross sections and properties in proton-proton collisions at $\sqrt{s} = 7$ TeV*, *Phys. Rev.* **D91** (2015), no. 11 112012 [1411.4969].

[48] **ALICE** Collaboration, D. D. Chinellato, *Consideration on normalisation*, March, 2016. Private communication.